Automotive side mirror surface contamination

An experimental study by Lagrangian Particle Tracking

MSc. Thesis

Tim van Puffelen

Delft University of Technology

TU Delft

Automotive side mirror surface contamination

An experimental study by Lagrangian Particle Tracking

by

Tim van Puffelen

to obtain the degree of Master of Science

at the Delft University of Technology,

to be defended publicly on Friday April 26th, 2024 at 09:30.

Student number:	4178556	
Project duration:	February, 2023 – March, 2024	
Supervisor:	Dr. A. Sciacchitano	
Thesis Committee:	Dr.ir. B.W. van Oudheusden	TU Delft, Chair
	Dr. A. Sciacchitano	TU Delft, Daily Supervisor
	Dr. M. Li	TU Delft
	Dr. T. Gericke	Volkswagen

Cover:	Droplet detachment around a side mirror [39]
Style:	TU Delft Report Style, with modifications by Daan Zwaneveld

An electronic version of this thesis is available at `http://repository.tudelft.nl/`.

TU Delft

Abstract

With the increased use of Advanced Driver Assistance Systems (ADAS) in modern cars, the field of surface contamination saw a resurgence. To keep the various sensors working properly it is of utmost importance to keep them clean and free of contamination. One way to achieve this is to ensure they are mounted in areas where they can be kept free of water droplets that can cause issues themselves, or by depositing contaminants that they are carrying. Current research focuses on the resulting contamination pattern after a drive or test on the car, this thesis however aims to see whether state-of-the-art Particle Image Velocimetry (PIV) techniques can be used to track the water droplets themselves, and with it open up new ways of researching surface contamination. To achieve this two experiments were performed. The first one was a simple experiment to see whether the droplets are being able to be imaged with the PIV cameras. The second experiment introduced a car side mirror model to the flow and used the Shake-the-Box (STB) algorithm to track the individual water droplets. Both of these experiments were successful, and showed that this combination of water droplets and STB PIV has great potential for being used in surface contamination research. The main issues found were with experimental setups, especially in the windtunnel. As the droplets do not follow the airflow accurately, extra care needs to be taken to ensure the droplets are operating at the right conditions, and are present at the measurement domain. The actual behaviour of the droplets as tracked by the STB algorithm, seems to be accurate with respect to the expectations indicating that the tracking of the droplets is accurate. Further research should try to increase the scale of the experiments, and/or introduce contaminants to the droplets to see how, if at all, this affects the traceability of the droplets.

Contents

Nomenclature

Abbreviations

Abbreviation	Definition
ADAS	Advanced Driver Assistance Systems
AFSB	Air Filled Soap Bubbles
FSU	Fluid Supply Unit
HFSB	Helium Filled Soap Bubbles
IPR	Iterative Particle Tracking
LED	Light Emitting Diode
LiDAR	Light Detection And Ranging
LPT	Langrangian Partilce Tracking
PIV	Particle Image Velocimetry
ppp	Particles per pixel
PTU	Programmable Timing Unit
PTV	Particle Tracking Velocimetry
RoF	Ring of Fire
STB	Shake-the-Box
SUV	Sports Utility Vehicle
...	

Symbols

Symbol	Definition	Unit
A	(Projected) Surface Area	$[m^2]$
C	Concentration	$[particles/cm^3]$
C_d	Drag Coefficient	$[-]$
d_diff	Diffraction Limit Diameter	$[mm]$
d_g	Geometric Diameter	$[mm]$
d_p	Particle Diameter	$[mm]$
d_z	Depth of View	$[mm]$
d_τ	Particle Image Diameter	$[mm]$
F_B	Buoyancy Force	$[N]$
F_D	Drag Force	$[N]$
F_g	Force of Gravity	$[N]$
$f\#$	F-stop	$[-]$
g	Gravitational Acceleration	$[m/s^2]$
I	Intensity	$[counts]$
M	Magnification Factor	$[-]$
N	Number of Particles	[-]
$\dot{N}$	Particle Production Rate	$[Particles/s]$
P	Pressure	$[bar]$
u	Velocity in x-direction $[m/s]$	
V_p	Particle Velocity	$[cm/s]$
V_t	Terminal Velocity	$[m/s]$
V_∞	Freestream Velocity	$[m/s]$
Δt	Time Interval	$[ms]$

Symbol	Definition	Unit
δz	Laser sheet thickness	[mm]
...		
λ	Wavelenght	[nm]
μ	Dynamic Viscosity	[$kgm^{-1}s^{-1}$]
$\rho_p f$	Fluid Density	[kg/m^3]
ρ_p	Particle Density	[kg/m^3]
τ_p	Particle Response Time	[s]
...		

1

Introduction

The issues of surface contamination of cars is as old as the car itself. Surface contamination can occur due to numerous factors, but is most commonly caused by wet road conditions and/or a dirty road surface. For years the main issues caused by the surface contamination was poor visibility if windows or the side mirrors were affected. If any other surface was affected aesthetics and possible transfer to driver and passengers when entering or exiting the vehicle were the main issues. In recent years however, in an effort to make cars safer and more autonomous, new cars have been fitted with an increased number of sensors. Most of these new sensors are fitted on the surface of the vehicle, therefore the research of surface contamination saw a surge in relevancy.

1.1. Problem Statement

One of the most widely used sensor in cars is the Light Detection and Ranging (LiDAR) sensor. LiDAR sensors use lasers to reflect off of objects back to sensor to measure distance between the object and the sensor. This is similar as how Radar works, only with lasers instead of radiowaves, this means the angular resolution is a lot higher [53], but LiDAR is a lot more sensitive to contamination effects. There are two ways to solve this, one is to get a quantification of the road wetness, and this can then let the sensor compensate for the current conditions. This is however a nontrivial matter, one could think rain sensors commonly found in cars might offer a solution, but these are limited to a certain range, and have no idea about the road conditions [61]. Therefore the second solution, which is to ensure that the surface of the LiDAR sensor is kept as clean as possible at all times, is the better fit to ensure proper functionality. To achieve this research needs to be done on the behaviour of contamination particles in certain critical areas of the car during it's design phase. Currently most contamination research is focused on the contamination patterns on the car after a driving stint (or a test run in a windtunnel). While these do offer good insight to were the contaminants are deposited, it gives little insight as to how and why they got there.

Particle Image Velocimetry (PIV) is a technique of measuring flows where particles are introduced to the flow. These particles are then illuminated with a strong light, and the reflections of this light are then caught by one or more cameras. This way the particles can be tracked over time and with that information the flow can be deduced. PIV is a relatively new technique, yet it has advanced rapidly to the point where currently individual particles can be tracked in large domains that allow for unscaled experiments with the use of for example the Shake-the-Box algorithm [58]. The current state of the art techniques all come together in the Ring of Fire (RoF) [68] as seen in figure 1.1. The RoF was initially developed for sports aerodynamics, and uses a tent filled with tracer particles through which a cyclist could pass through, and the flow is then measured by tracking the movement of the particles with PIV. This concept can however be extended to cars and other larger vehicles.

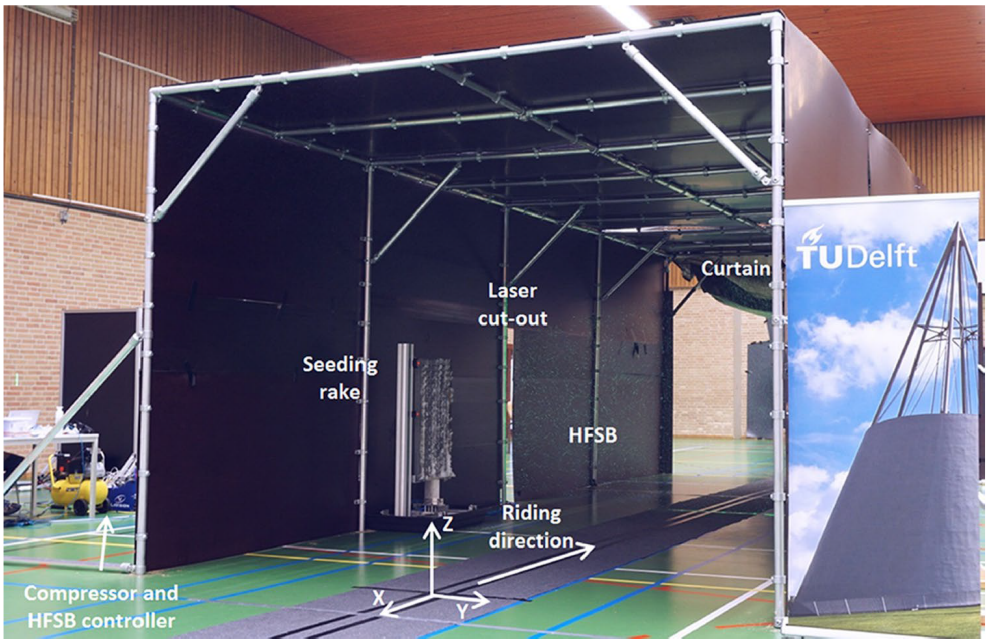

Figure 1.1: Ring of Fire setup as used by [64]

Generally PIV has been used with particles that have a low response time in the flow and are neutrally buoyant so there movement is as close to the movement of the flow as possible as that is what needed to be measured. This technique could however also be used to track particles that are heavier than air with high response times, for example water droplets. While this means the flow will not be represented by the movement of the particles, the exact movement of the water droplets can be tracked. This is exactly what was missing in the current research of contamination: A way of tracking droplets to see how they arrive at the car surfaces.

1.2. Thesis Objectives

As described above, the use of water droplets as seeding particles for the purpose of surface contamination research is a promising new technique to further advancements in surface contamination research. If successful this could lead to new ways to research contamination from the source and track it all the way to wherever it is deposited. As such a research objective and research question(s) can be formulated.

The main objective of the research are to determine whether water droplets can be tracked by state-of-the-art Lagrangian Particle Tracking (LPT) algorithms by assessing their trajectories for the flow around a car side mirror.

The main research question is:

- **How effective are water droplets as a seeding particle for surface contamination PIV experiments in combination with the Shake-the-Box algorithm?**

The sub-questions to guide the research to answering the main question are:

- **How well are the cameras able to image the droplets?** As PIV works by reflecting light off of the tracer particles, it needs to be determined whether water droplets reflect enough light back to the cameras to be detected.
- **How well does the Shake-the-Box algorithm track the droplets over time?** The STB algorithm uses the particles motion over previous frames to predict the particles position in the next frame, this means the water droplets need a fairly consistent behaviour to be able to be tracked.
- **How are the trajectories of the water droplets affected by the presence of a model in the**

flow, such as a side mirror? Introducing a model in the flow and see how the droplets and the tracking of them is affected gives a lot of information on how the droplets behave in a realistic test scenario.

1.3. Thesis Outline

The theoretical background on surface contamination and spray can be found in chapter 2, the background knowledge for PIV can be found in chapter 3. In these chapters the history of research in these areas is discussed as well as the current state-of-the-art techniques currently in use. Chapter 4 discusses the two experiments performed for this thesis, the first on being a spray characterization experiment to see how well, if at all, the droplets can be tracked in a PIV experiment. The second experiment was a more relevant test case where a car side mirror model was introduced to the flow with the water droplets. The results of both these experiments can be found in chapter 5, where they are also interpreted and their validity is discussed as well. Finally the conclusions and recommendations for further research can be found in chapter 6.

2

Soiling in Automotive

2.1. Contamination

This section aims to show what contamination of vehicles is, and what effects it has on the vehicle and its user(s). This includes a description of contamination and how it occurs, followed by a overview of the various effects it can have on the vehicle, the driver, and any Advanced Driver Assistance Systems (ADAS) in use. Furthermore a short overview of the history of contamination research is given including an overview of the current state of this research and its prospects into the future.

2.1.1. Types of contamination

Contamination of a vehicle's surfaces can happen by various means, in general this occurs due to weather and/or road conditions such as rain, snow and dust. The contaminant then adheres to the surface of the vehicle while driving, leading to the surfaces becoming contaminated. An example of the resulting contamination is seen in figure 2.1. Hagemeier, Hartmann, and Thévenin [28] described three main sources of contamination, which is also shown graphically in figure 2.2:

- Primary contamination
- Foreign or 3rd party contamination
- Self-soiling

Figure 2.1: An example of contamination on the side surface of a car [70]

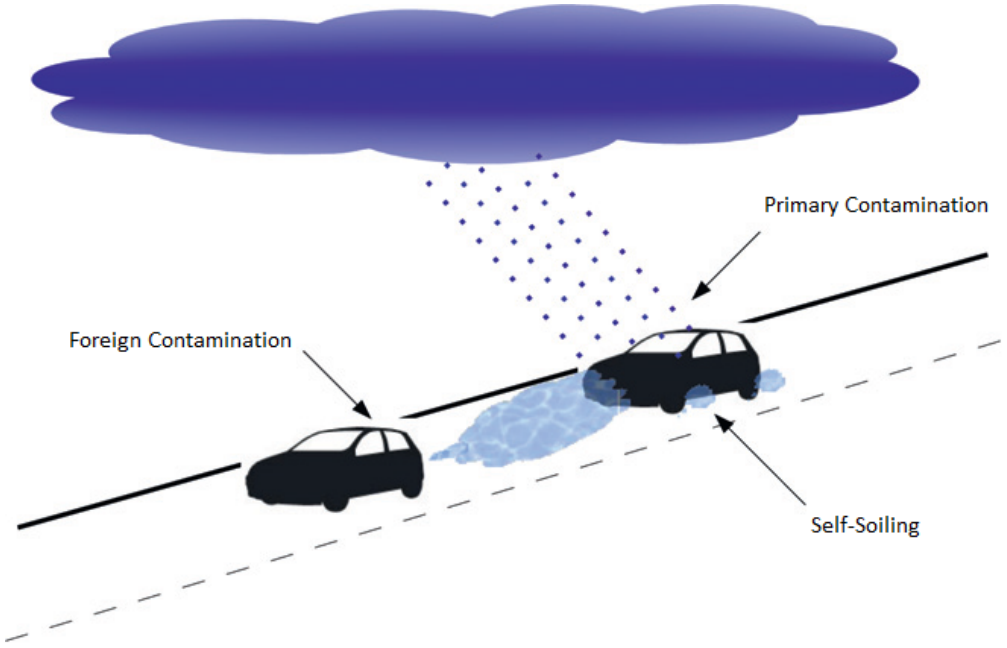

Figure 2.2: The three origins of contamination [28]

Primary contamination is described as the contamination coming directly from the environment, this includes rain and snow falling from the sky onto surfaces of the car. This primary contamination mostly affects the top surfaces of the car. Foreign contamination however is caused by other road users, for example the spray coming from a car ahead. Depending on where the source is situated this type of contamination can affect all surfaces of the car. Lastly there is self-soiling, this occurs when driving a car on a wet or dirty surface. The wheels of the car pick up contaminants from the road, and release them into the air close to the car's surface, where they are picked up and deposited further along the surface. Self-soiling mostly affects the sides of the car due to the front wheels, and the rear surface due to the rear wheels and floor of the car. The rear contamination is most notable on blunt rear vehicles such as SUV's and station cars due to the blunt rear causing strong recirculating vortices to form which

deposit the contaminant on the rear surface [21]. Figure 2.3 shows the spots that are most affected by self soiling on a basic car model.

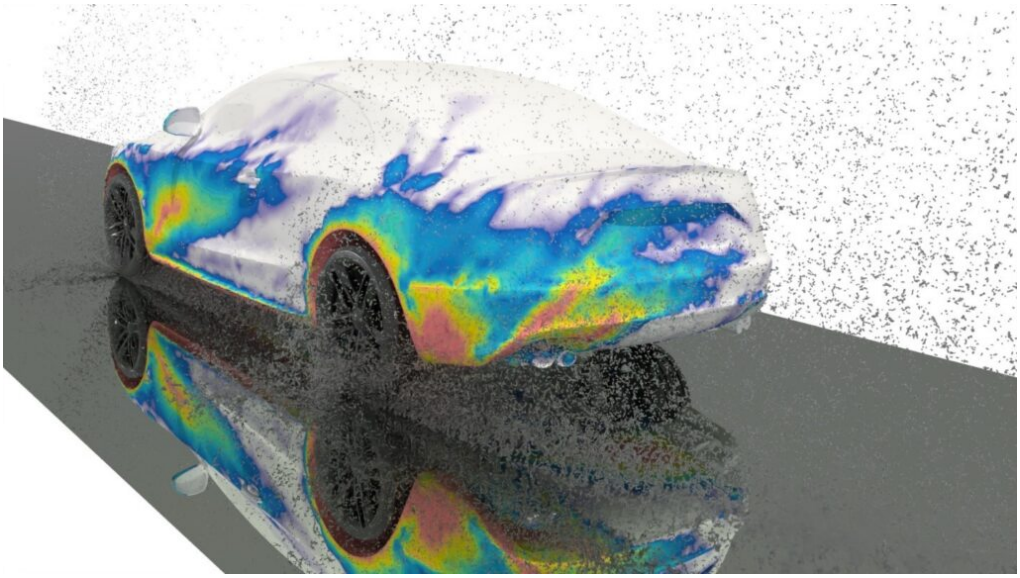

Figure 2.3: An example of self-soiling hotspots on the side and rear surface of a car [63]

While water is generally considered the most common form of contamination, there tend to be a lot of contaminants in or carried by the water that can alter their effect on the surface, this is mostly true for the foreign and self contamination as most of these contaminants emanate from the road surface. These contaminants include obvious examples such as natural soil, desert sand, ocean salt etc. But can also include Biogenic material, grit and de-icing salt as well as particles produced by other vehicles, such as combustion particles, oil, brake dust, cleaning agents and tire particulates. This is of course not an all encompassing list, but shows the wide variety of substances that can be in or carried by water and deposited onto the vehicle.

2.1.2. Effects of contamination

Aside from the obvious aesthetic effects, some of the most notable effects of contamination include degrading lighting, obstructing visibility, degradation of glass due to abrasion, and wiper wear [23] as well as degraded ADAS performance, degraded brake performance and transfer of contaminants to clothes and hands when entering or exiting the car [31][66]. The effects of each of these on the vehicle and driver can vary quite a bit in severity, from minor inconveniences to severe safety hazards, especially considering the fact that cars are rapidly becoming more dependent on ADAS for either safety or to allow for autonomous driving in the future. These systems can for example give false positives on collision and blind spot detection [36] which can cause unintended and potentially dangerous situations to occur.

The way contaminants like dust and snow decrease visibility is fairly obvious as they are opaque, and therefore obstruct the view. For water droplets this is a bit different, as they are transparent, but due to the way they reflect light they also decrease the visibility for any observer [28]. The areas of a car that provide the highest risk on impacting safety if contaminated are the Windshield, Side Window, Side Mirror and the A-pillar which serves as the boundary between the windshield and side window[2]. While wipers can clean the windshield, they mostly displace the water to the sides of the car, resulting in more water on the side windows and mirrors decreasing visibility there [28]. This effect is called A-pillar overflow, as shown in figure 2.4, and is also one of the main sources for mirror contamination, the other being droplet detachment from the mirror's own housing [39].

Figure 2.4: A-pillar Overflow visualized [36]

The effect on ADAS can also be significant, for example when looking at one of the most used ADAS systems: LiDAR, which, compared to mm Radar systems has a higher angular resolution in the azimuth plane ($< 1deg$) [53] but is more sensitive to contamination effects. LiDAR is used for many automotive

applications including pedestrian safety [73] and autonomous driving [11]. LiDAR systems are particularly sensitive to contaminations [53]. Rasshofer, Spies, and Spies[53] and Filgueira et al.[17] found the maximum range of LiDAR can be reduced by up to 50%, Hasirlioglu et al.[29] [30] showed that rain causes a reduction in contrast, which results in more difficulty to find objects. These studies mostly tested for environmental effects on LiDAR, Trierweiler et al.[71] looked at the effect of contamination on the sensor cover and found a maximum range reduction of up to 75%. Fersch et al.[16] found that LiDAR sensors are most affected by smaller drops due to their larger fill factor (up to 55% reduction in power received), they also found a minimum attenuation when drops were half the diameter of the laser (25% reduction in power received). Similarly Shearman, Hoare, and Hutton[62] found an attenuation of up to 20dB for a 24 meter roundtrip distance when looking at the spray produced by a lorry. This shows that LiDAR is severely affected by rain and contamination, and that contamination control can alleviate this issue a lot.

2.1.3. Current state-of-the-art research on automotive contamination

Solutions for keeping the windshield of a car clean have been there for a long time, starting with the hand operated rain rubber [35], which eventually evolved into the integral wiper systems widely in use today. Surface contamination of other surfaces was however more of a concern in aeronautical industry. From the 1960's onward concerns regarding surface contamination for road-going vehicles grew. Some of the problems that were mainly considered were preventing the overflow of the windscreen onto the side windows and from the roof onto the rear panel as well as trying to minimize the contamination of the body panels, mirrors and lamps. One of the first studies was done by Morgan W Dawley [12] where it was found that the flow separated behind a stationwagon, and stated that the wake caused by this separation picks up mud and dust from the road and thereby contaminates the rear surface. Later studies done by G Maycock [45], Weir et al. [75] and Costelli [10] found that the box shape of certain cars, such as SUV's, stations, trucks and hatchbacks, are particularly prone to having their rear surface contaminated. Some of the early solutions aimed at alleviating this include turning vanes at the trailing edge of the roof to reduce the surface contamination on the rear, however it was later found that these can increase drag by up to 20% [25] [51]. These solutions also generated a lot of noise, so eventually focus shifted to solutions with a lower impact on drag and acoustics.

Through the 1980's and 1990's a lot of research was done to try and limit the amount of spray coming from a vehicle, for example Olson and Fry [47] tried to reduce spray by treating the wheel arch and adding fenders. Similarly heavy duty vehicles were given flaps to reduce the third party contamination they produce [1]. Lajos, Preszler, and Finta [40] found that the contamination of rear surfaces was mostly dependant on the rear wake and underbody flow. The analysis of more complex flows such as around the side mirrors also started to gain traction, for example Waki et al. [72] visualized the flow around a car mirror focusing on rain contamination and wind noise.

In the early 2000's the work on contamination continued with looking at self contamination with solid dirt particles [78], as well as numerical simulations starting to become viable for predicting soiling patterns [5]. Characterizations of spray also became more useful as the numerical solutions such as done by Bouchet, Delpech, and Palier [6]became more popular. Some other research also found that overall aero improvements can reduce spray as well, leading to more efficient solutions that don't clash as much with other design drivers [74] [44]. As an example of the progress made, Volvo had a solution for the V70 which used a ducted rear spoiler to reduce dirt by 15% without increasing drag[34].

From the 2010's onward research in contamination accelerated as not only safety requirements were still increasing, also the use of ADAS became more commonplace. Some of the early results gave indirect evidence to the fact that self-soiling is mostly spray splashing on the wheel house, and not spray from the wheels themselves [21]. It was also found that small changes on the geometry can have a big impact on the contamination pattern [23], and therefore should be incorporated into the design cycle as early as possible [21]. A lot of experimental studies were done with UV-doped water, for example by Gaylard et al. [23] and Kabanovs et al. [37]. While this way of measuring gives a good insight on the resulting contamination patterns, the results are mostly qualitative [28] [31]. As a result there was a need to get more quantitative results, Hodgson et al. [31] developed a method of converting the grayscale of an image into fluid depth values by using a calibration vessel. Most of these studies tend to focus on the contamination pattern after a test. Less focus is on how the contamination

travels from the source onto the contaminated surface. Of note is also the fact that all these test are done with either clean or UV-doped water, while the added mass of solids in the water droplets can affect their trajectory significantly.

Some of the most useful conclusions, from all these years of research include the fact that the side soiling height can be reduced by reducing the favourable pressure gradient between wheel house and the side body [52],[49]. It was also shown that droplets impacting the mirror housing are deposited on the side mirror obscuring view [2]. Finally it was found that rear soiling is dependant on pressure in the rear wake, where a higher surface pressure means an increase in soiling [10]. One of the more complex areas, where there is still a lot of research to be done is around the A-pillar [22], the complexity of this area can be seen from figure 2.5.

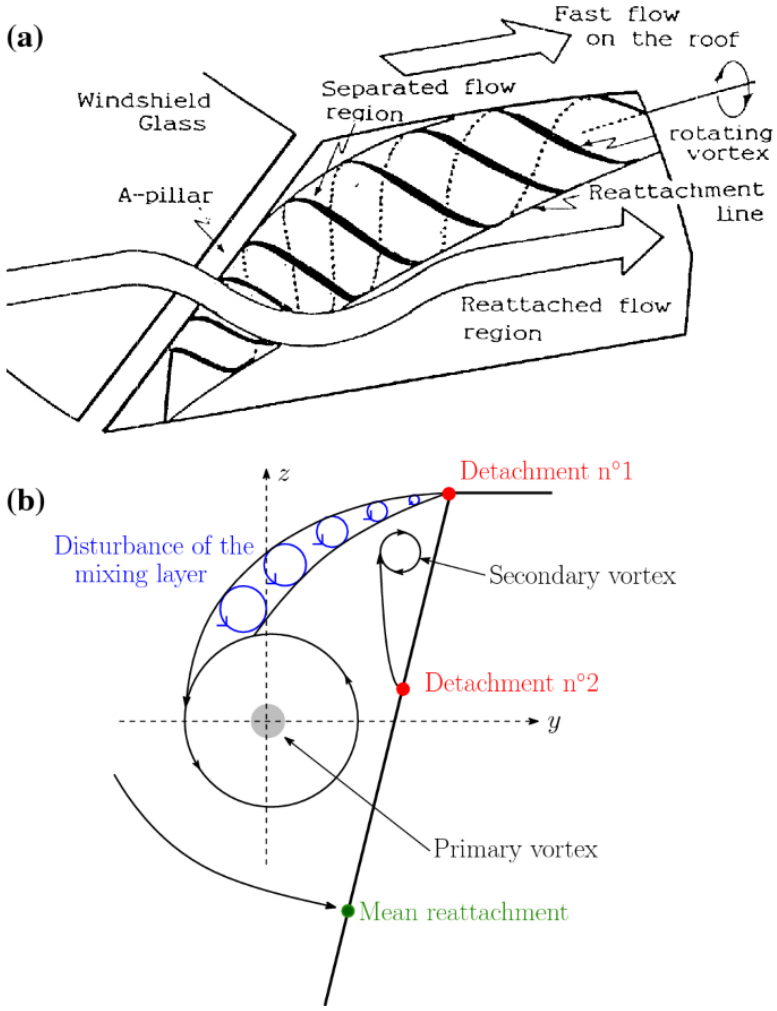

Figure 2.5: Visualization of the complexity of the flow around the A-pillar [18]

Several ways of measuring contamination have been employed. The most obvious one being the test track with a running car. While maybe the most straightforward test case, there are some limitations to using a test track. First of all a running vehicle is needed, which depending on where in the development cycle the vehicle is may not always be available. If they are available they are at risk of exposure, which for prototype vehicles is generally something that companies want to avoid. Furthermore there are the environmental conditions which can not be controlled at the track, resulting in wide swings of conditions and as a result potentially unreliable data. Lastly the actual measuring is a bit more complicated as not all types of measuring devices are suitable to be taken/used at a track. At the track there are various ways of creating/simulating spray, for example using troughs filled with water as done by Maycock [45] as well as Goetz and Schoch[26], as well as using an upstream car with a spray grid[2]. To get more

dirt the use of a wetted gravel road has also been used [12] [51]. To measure for example the soiling on the side mirror photosensitive paper has been used [72].

Windtunnels have also been widely used, but they have their own limitations. One of the main advantages is that they can be used earlier in the development cycle. One of the main drawbacks is the fact that most aero-tunnels' ground-systems are not suited for large amounts of water, which are needed for proper spray simulations. Using Climatic tunnels also tends to be difficult as they tend to have smaller test sections to keep better control of the conditions, but this increases the boundary effects of the tunnel on the model. There are some newer climatic tunnels that include spray systems and boundary layer control [4] [3], although these are still not suited for simulating tire spray. The ideal combination of aero ground systems and tire spray generation is therefore still not available. There are two ways of generating spray in a windtunnel, first is the third-party spray which can be generated via a grid of nozzles as seen in figure 2.6, a close-up of one of these nozzles can be seen in figure 2.8. The second option is to generate tire spray by depositing water in front of a rolling tire as shown in figure 2.7.

Figure 2.6: Example of a third party spray generator [22]

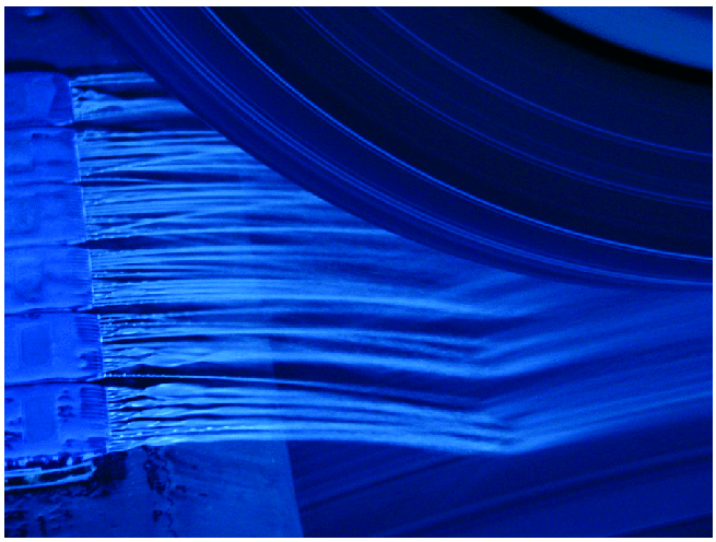

Figure 2.7: Example of a tire spray generator [22]

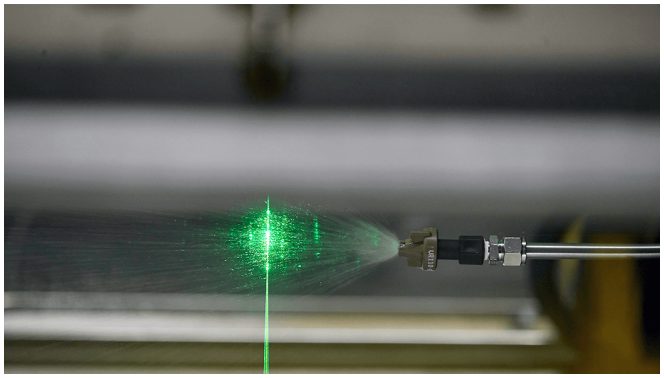

Figure 2.8: Closeup of an example of a spray nozzle [41]

2.2. Spray

This section aims to give an overview of what spray is, how it is formed and what different types of spray can exist. A small overview of what certain conditions can change the form the spray takes, including velocity, tire tread and road surface is given. Lastly a small overview of quantifying road wetness and spray intensity is also given as these have a big impact on how ADAS can function.

2.2.1. Different types of spray

What is commonly called spray can be divided into two generic categories, referred to as splash and spray. Splash consists of larger droplets that have a ballistic trajectory i.e. they do not follow the flow at all. Spray is made up of smaller droplets that are at least partially carried by the flow [75, 32]. A tire has 4 distinct areas where splash and spray are generated, splash is generated as the bow and side splash waves. Spray is generated by tread pickup (also named torrent spray) and capillary adhesion (also named circumferential spray) [69]. figure 2.9 shows all four of the categories as generated by a tire.

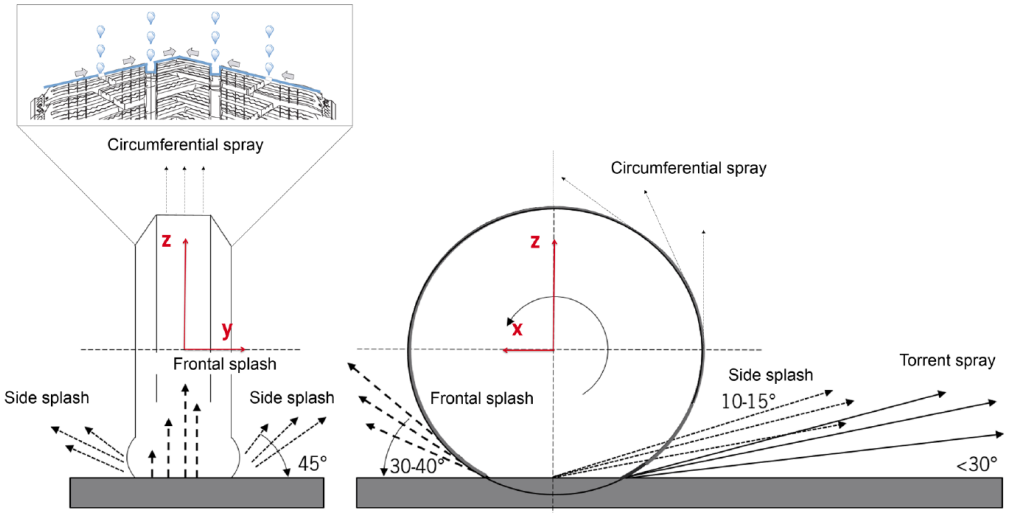

Figure 2.9: The four categories of splash and spray [61]

The bow and side splash waves are caused by the fact that a tire will push the water film on the road away from the contact patch, slick tires would push everything away, whereas treaded tires can push it into the grooves [61] which increases the depth of the water film needed before aquaplaning (when the tire is lifted from the road by the water) occurs. Spray is generated by two mechanisms, first the torrent spray comes out of the back of the contact patch of the tire at a shallow angle, and only at high wetness levels, this is mostly formed due to the tire grooves[61] through which the water is pushed as the tire

rolls. Circumferential spray is basically the spray that sticks to the tire and therefore is not released as torrent spray and follows the tire surface longer, the droplets then leave the surface as they reach the upper parts of the tire and get caught in the airflow [75].

2.2.2. Droplet size

The droplet diameter distribution is affected mostly by the road, velocity and tire [65, 21, 19]. The influence of speed is mostly that higher rotational velocities cause smaller droplets to be released compared to lower velocities [27, 52]. figure 2.10 and figure 2.11 show the droplet diameter distribution for a lorry at 60 miles per hour as measured by Shearman et al. [62] and Borg and Vervang [5] respectively. figure 2.10 shows that purely based on count the smaller droplets are the dominant ones, figure 2.11 shows that if you are closer to the origin of the spray larger droplets become slightly more common, which is as expected, as larger (and thus heavier) droplets tend to fall on the ground a lot earlier than the smaller and lighter ones which are (partially) carried by the airflow. A similar experiment for a car was done by Bouchet er al. [6] for different velocities for a car as shown in figure 2.12. This study shows that as speeds increase the distribution of droplet diameters shift to the smaller droplets, although the droplet diameter at which the peak occurs doesn't shift all that much, the peak does get significantly smaller and the amount of droplets smaller than this diameter increase by a lot as well.

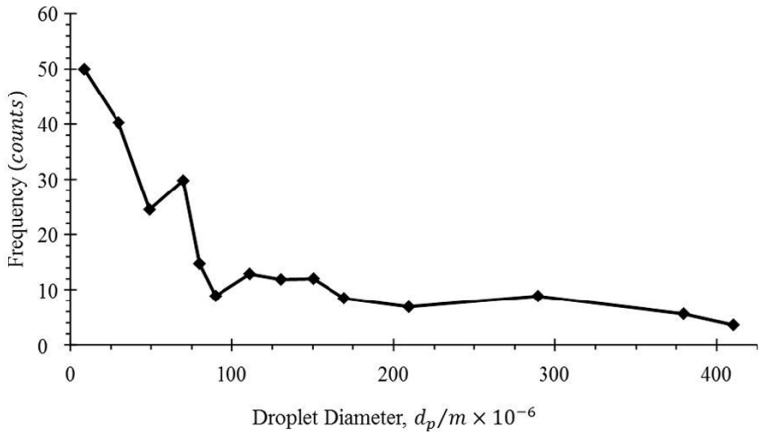

Figure 2.10: Droplet diameter distribution as measured by [62]

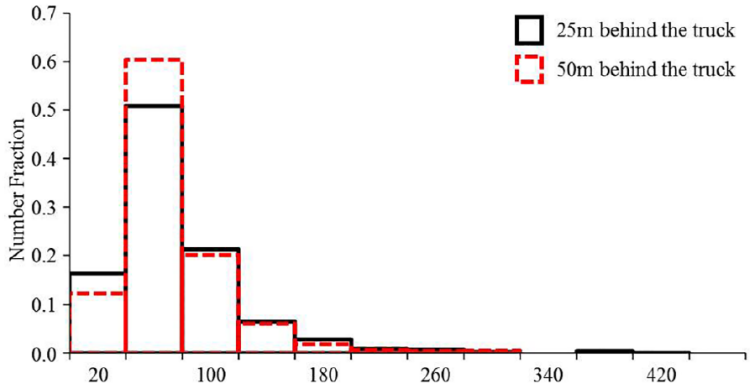

Figure 2.11: Droplet diameter distribution as measured by [5]

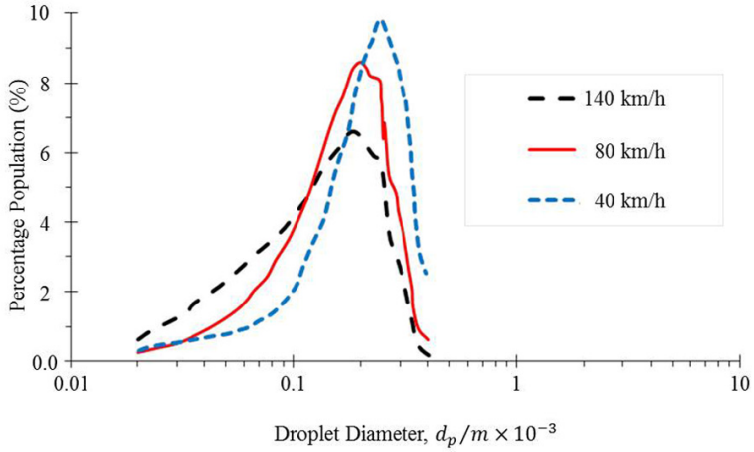

Figure 2.12: Droplet diameter distribution as measured by [6]

2.2.3. Spray formation

A good visualization of how spray is formed due to the grooves of tires (mostly torrent spray) is shown in figure 2.13 [52]. Radovich and Plocher used two tires stacked against each other instead of a tire on a surface, but the principal stays the same.

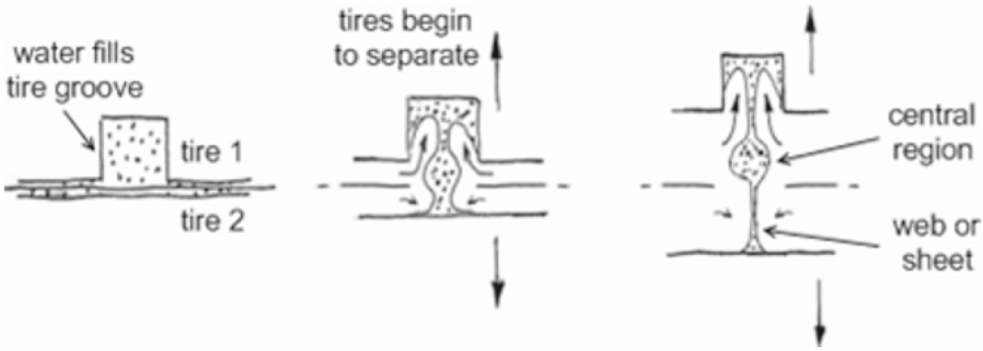

Figure 2.13: Droplet formation in a tire groove [52]

Water is captured in the groove at the contact patch, as the water follows the tire it starts to get stretched between the surface (in this case another tire) and the tire, eventually breaking up into droplets. The diameter of these droplets depends mainly on the thickness of the webs and sheets that are created as the water is stretched [52]. As one can imagine, these sheets and webs become thinner as the velocity increases as the water is stretched harder, therefore creating smaller droplets. Similar behavior is caused by thinner and deeper grooves, as they cause the water to be in a more elongated shape before the tire leaves the surface, essentially 'pre-stretching' the water.

2.2.4. The effect of spray on ADAS

As discussed in section 2.1, the performance of ADAS is deteriorated by contamination, which spray is a major contributor to. To compensate for this a possibility is to have the ADAS know how much spray it is receiving and compensating for that. While this is to a certain degree fairly simple for humans, it's non-trivial for these systems. There are rain sensors already in use for cars, but these are only used for activating the wipers, as a result they can not quantify intensities above a certain limit [7], and have no idea about what the road conditions are [61]. This means that while the rain sensors may detect heavy rain, the road could be drained well and spray could therefore be not too much of a problem. The opposite could also be true, where puddles are present from a previous rain shower causing spray,

yet no rain is detected by the sensors. Furthermore, using front cameras is similar as using the human eye, good for a qualitative assessment, but not good for a quantitative analysis [61], rear view cameras can in theory use the spray and carvings made by the tires into the water film to get a quantitative measurement. The problem with this solution is the fact that these rear cameras are reliant on daylight to do this accurately, at night the spray is hard to track with normal cameras due to the headlights of following vehicles [60].

There are some systems that can quantify road wetness, for example the MARWIS by Lufft [43] and Road eye by Optic Sensors [54], but these are either too large and/or expensive to be mass-produced at the moment. As a result it is still very difficult to get a road wetness quantification for mass-produced cars.

3

Particle Image Velocimetry

This section aims to show the basics of how Particle Image Velocimetry (PIV) evolved over the years to become a measurement technique that is especially useful for the current contamination research. This includes a brief explanation on the basic principles, followed by the history of how it evolved over time to the powerful technique that it is now. In the end the newest developments including Shake-The-Box and the Ring of Fire are covered, as these especially are interesting for the current investigation.

3.1. PIV Basics

PIV is a technique where particles (generally neutrally buoyant in the flow medium) are introduced to the flow. These are then illuminated (usually by a laser) and multiple images are taken at short time intervals. The movement of groups of particles between two successive frames, generally calculated via cross-correlating areas of the images, then indicates the flow at that location. A basic (planar) PIV-Setup can be found in figure 3.1 There are some conditions these particles need to meet to be good candidates for PIV.

- The concentration of particles should be limited such that no multi-phase flow effect occur, this is dictated by the mass ratio of the fluid and the particles
- The particles must be randomly distributed to ensure no biases are present
- The particles need to be clearly detectable with an imaging device when illuminated
- The particles time response (time it takes for a particle to adapt to a change in velocity) should be smaller than the smallest time scale of the flow, ensuring the flow is captured well by the particle movement.
- The particles should not be harmful to any of the experimenters and objects/devices present in the testing facility.

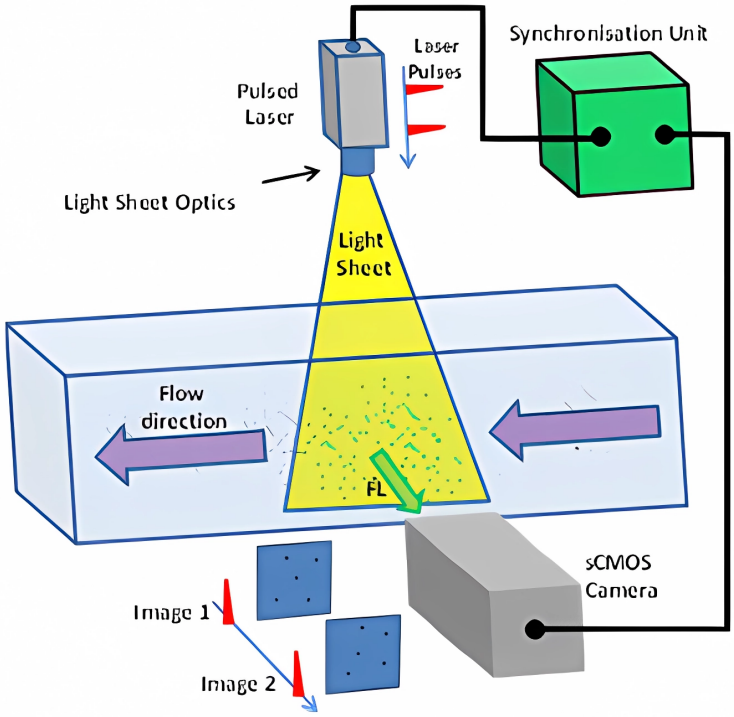

Figure 3.1: An example of a PIV setup [48]

PIV has multiple sub-categories that are widely used:

- Planar/Stereo PIV is the simplest form of PIV, where a thin laser sheet is created to illuminate the particles, this then gives a 2D view of the flow with either two velocity components (Planar) or three velocity velocity components (Stereo).
- Tomo-PIV uses more cameras and a thicker laser sheet to capture three velocity components in a 3D domain.
- Shake-the-Box/4D Particle Tracking Velocimetry (PTV) traces each individual particle over time instead of using a cross correlation on interrogation cells containing multiple particles.

The main benefit of PIV compared to more traditional methods is the fact that it is non-intrusive and therefore lends itself well for more complex flows. Although for turbulence and other inherent 3D flows the planar PIV can not provide any information out of the plane of measurement, and can suffer from errors due to the out-of-plane motion of the particles. The main drawback of PIV is that even for the simpler forms, setups can be quite complex and prone to errors due to small disturbances.

The growth of PIV has been very rapid, as domains have gone up from $10x10cm^2$ in the mid 90's to $50x50cm^2$ by 2015 [57]. Patching multiple domains together to get even larger ones has also been done [8] [42]. As PIV became more widespread, naturally the interest would shift towards using it for 3D flows, as the non-intrusive nature of PIV lends itself perfectly to measuring turbulent flows.

3.2. Example PIV Results

To show what can be achieved with PIV, this section shows some examples from various PIV experiments in different areas of research. A relatively simple planar PIV setup can be used to determine the average flow field in the plane of measurement. This average flowfield can then be shown as for example velocity or vorticity contours and streamlines, as shown in figures 3.2a and 3.2b. A more complex Tomo-PIV setup allows for a 3D measurement domain, this means 3D structures can be shown, for example isosurfaces of velocity as shown in figure 3.3a. Using a particle tracking algorithm allows for each particle to be tracked over time, this allows for the particles to be traced over time, as is shown in figure 3.3b.

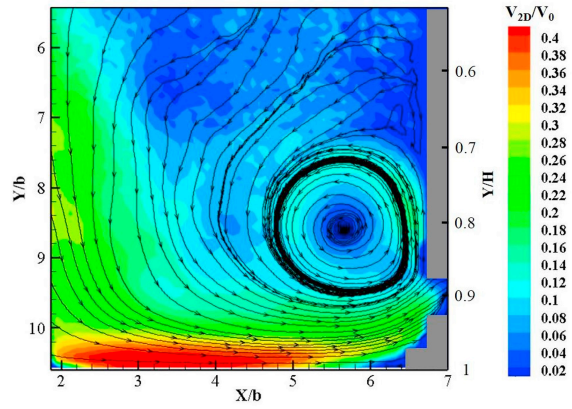

(a) Dimensionless contours of the 2D mean velocity in the stagnation region of a selective laser melting (SLM) working chamber obtained with PIV. [9]

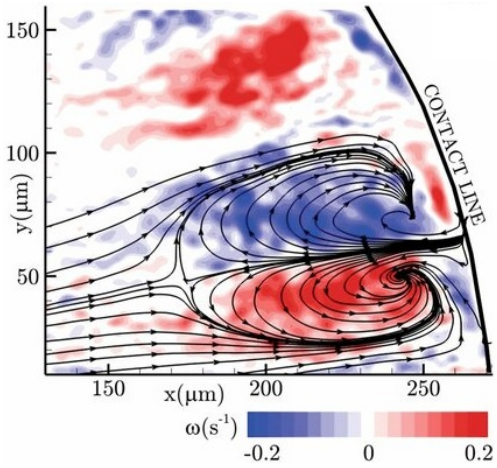

(b) Time averaged Vorticity field of jet-like vortex structures near the contact line of an evaporating sessile droplet superimposed with the velocity streamlines.[24]

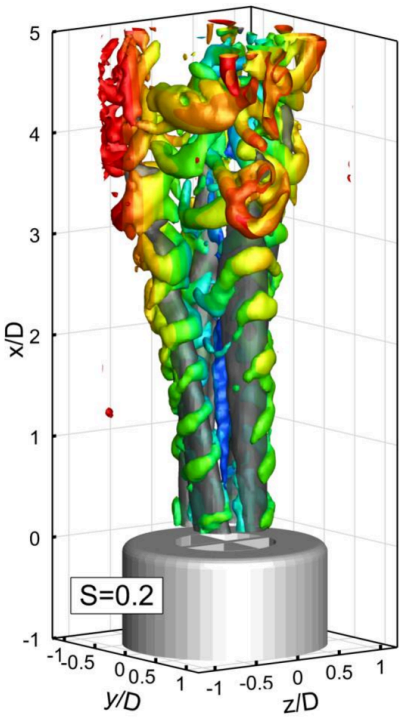

t $S = 0.2$. Isosurfaces of axial velocity ($u/U = 0.7$, dar

(a) Instantaneous flowfield of swirling jet, color coded by distance from center.[55]

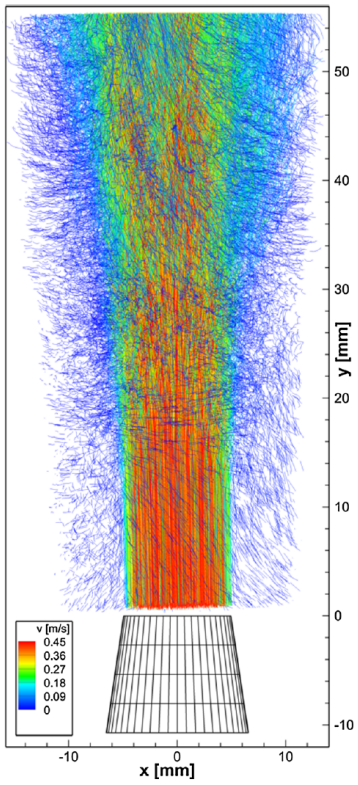

(b) Particle tracks of a water jet, color coded by velocity.[58]

3.3. 3D PIV

The move to 3D PIV Techniques initially started with three variants: 3D PTV, Scanning Light Sheet (SLS), and Holographic PIV. All of these techniques had their own flaws and were therefore not widely used. The first 3D PIV technique that did achieve a more widespread use was Tomographic PIV (Tomo-PIV).

The initial research that showed the capabilities of Tomo-PIV was performed by Elsinga et al. [13]. Tomo-PIV works by expanding the laser sheet over the third dimension to cover a greater depth, generally roughly a quarter of the width or length of the laser sheet. Multiple cameras at different angles

are collecting the light scattered of the particles. The true novelty of tomo-PIV is the tomographic 3D reconstruction of the domain allowing for the actual PIV to be done in the 3D domain. At first Tomo-PIV domains were fairly small, starting at around $13cm^2$ by Elsinga et al. [13], but rose over the years up to $16x22x8cm$ by Fukuchi [20]. The main drawback of Tomo-PIV was the fact that the laser light had to be expanded a lot more and thus the intensity of the light scattered by the tracer particles was severely diminished. Combine this with the fact that the cameras need to operate with a higher f# (Ratio of focal length and aperture diameter indicating the light gathering capability of the camera) due to the increased depth of field required and the problem only gets worse [57]. In general a doubling in the depth of field results in an order of magnitude reduction in intensity received by the sensor [57].

A solution to this problem was to have tracer particles that could scatter more efficiently, Scarano et al. came to Helium Filled Soap Bubbles (HFSB) [57]. HFSB have been used before, as early as 1956 [50], where they were used to visualize path lines at low concentrations. They were also shown to persist all the way up to Mach 0.9 [33], making them suitable for a lot of applications. An uncertainty study on these tracers was done by Kerho and Bragg [38], they concluded that HFSB were not suited for visualizing streamlines unless neutral buoyancy was achieved. This was at that point in time not possible, as the device used filtered out the heavier than air particles, leaving the average at lighter than air. Since then HFSB have still been used, but mostly in low speed flows and for qualitative results. Scarano et al. [57] showed that with sub mm bubbles that are neutrally buoyant a characteristic response time in the order of $10\mu s$ can be achieved with a similar setup to that of Kerho and Bragg [38], making HFSB suitable for quantitative measurements. HFSB tracers quickly let measurement domains grow, up to sizes like $2m^2$ at $4m/s$ [67] and $0.5m^3$ [58].

With one of the limitations removed, Tomo-PIV still has some flaws. First of all the high degree of precision needed, means calibrations and experiment set-up is very precise, and if done incorrectly or sub-optimally, the results could be skewed by a significant amount fairly easily. Even when everything is done with the upmost care, mapping errors can still be as large as $0.5 - 2px$, where a precision of $< 0.1px$ is preferred ($< 0.4px$ required)[77]. Volumetric self-calibration as presented by Wieneke et al. [77] shows the process of self-calibration, this uses the images with the tracer particles present to dewarp them to the $z = 0$ plane, which corresponds to the normal calibration. Cross-correlation is then performed to match these two, when the disparity vector field is zero the two images are matched. Using this volume self-calibration calibration errors of $1 - 2px$ have been reduced to $0.1 - 0.2px$ [77].

3.4. Particle detection

The last issue Tomo-PIV faces is on the analysis side. Not only does it require a large amount of computational burden, the formation of ghost particles makes the analysis also a lot more difficult for higher seeding densities. Ghost particles are formed when two or more cameras create a false positive at locations where no actual particles are present see figure 3.4.

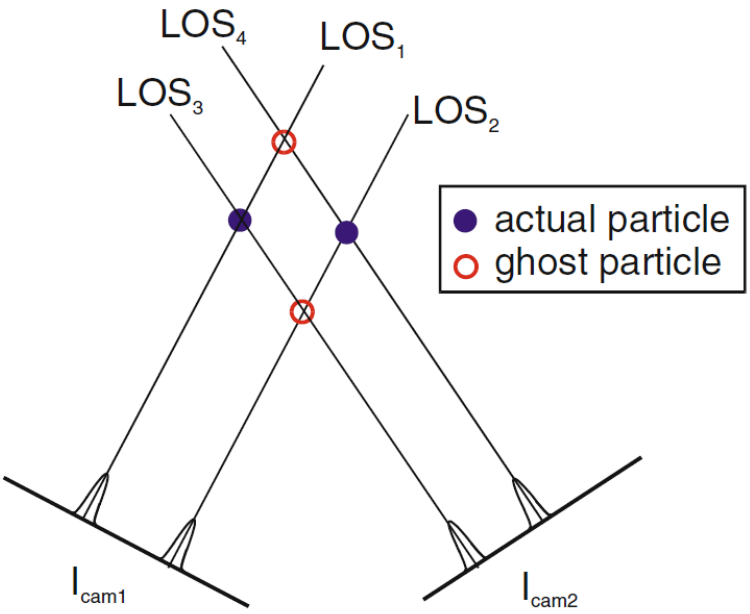

Figure 3.4: Ghost particle formation [14]

As ghost particles are created by multiple particles in the same region, these particles tend to stay for multiple frames. Were they to stay for only 1 frame, they would not influence the velocity field [14] as the velocity field is calculated using multiple frames. As the ghost particles tend to travel with the particles that created them, they tend to smooth out the velocity gradient. Ghost particles tend to be relatively short lived as the movement through the domain causes the camera angles to change to such an extend that the ghost particles do not exist at those locations anymore, however this does also mean new ghost particles can be formed by that point. The formation of ghost particles meant Tomo-PIV had to work with relatively low seeding densities. Densities lower than 0.022 particles per pixel (ppp) would not work, as that would be too sparse to gain information. Tomo-PIV works for up to 0.1 ppp, although it works best around 0.055ppp [56]. The last part of the analysis side that limits Tomo-PIV is the fact that it averages values over an interrogation window that is used for the cross-correlation, this window can not be made arbitrarily small as this would affect the accuracy due to too few particles being present in the interrogation windows if they are taken too small. As a result the spatial resolution is limited, making it less effective near large velocity gradients. One of the solutions to alleviate this problem is to use 3D Particle Tracking Velocimetry (3D PTV), this tracks each particle individually instead of using cross correlation. The biggest problem with 3D PTV is that it is very sensitive to overlapping particles, requiring seeding densities to be even lower than Tomo-PIV (by an order of magnitude) [46].

A new technique called Iterative Particle Tracking (IPR) [76] alleviated this issue. IPR is basically a hybrid between Tomo-PIV and 3D PTV, similarly to Tomo-PIV it iteratively reconstructs the particle locations by comparing the recorded images with projections calculated using the particle distribution in the volume. It does however represent the particles as objects in a position like 3D PTV, as opposed to Tomo-PIV that creates voxel based intensity blobs. This opened the door to using higher seeding densities with 3D PTV, comparable to Tomo-PIV. Quickly came an improvement to IPR, namely Shake-the-Box (STB) [58], which was initially described as 4D-PTV (time-resolved 3D PTV). While IPR reconstructs the particles position every frame, STB aims to use the obtained velocity information to predict the particle locations in the next frame. STB starts with IPR for the first few frames, then uses the velocity field it calculated from these initial frames to predict the next location of the particle, then 'shakes' this prediction in space till it coincides with the actual location of the particle, a visual explainer of this algorithm is shown in figure 3.5. This process inherently eliminates ghost particles that don't follow a coherent path, ghost particles that form in particle 'clouds' that therefore do follow a coherent part are not eliminated.

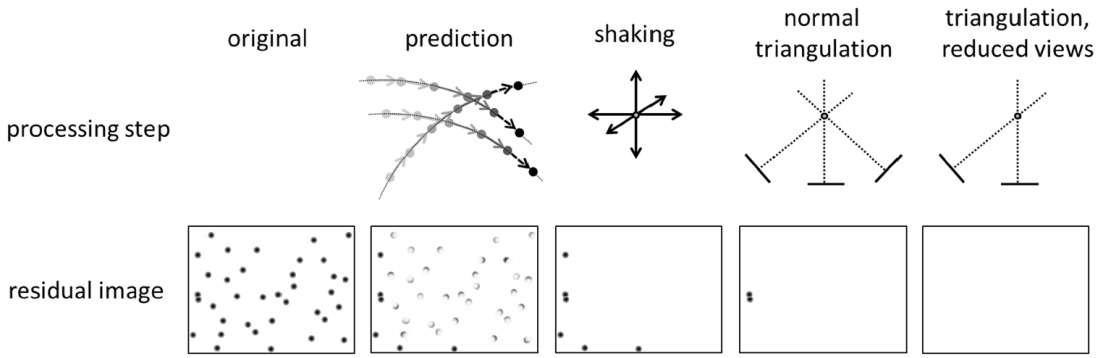

Figure 3.5: Visual explainer of the Shake-The-Box Algorithm [58]

STB does not only have a higher accuracy than voxel based correlation techniques, but also less of a computational burden [46], making it really useful for large amounts of data. As an additional step to increase the accuracy STB can also be ran backwards to locate tracks that might have had incomplete data early on, possibly finding extra tracks [58]. The dependency of STB on the velocity field of the previous frame to predict the particle locations in the next frame, means it has problems with flows where high velocity variances are present. Typically data acquisition is done at the frequency needed to find the fastest particles. This means that significantly slower particles are potenitially perceived as stationary. To alleviate this issue Multiple passes at different time-separations can be done [59] covering a different velocity regime with each pass. One thing to note here is that it is very beneficial to also do a back and forth on these time-separations to find particles that are both going up and down into new velocity regimes [59].

3.5. Ring of Fire

One innovation to PIV that has recently been made is the Ring of Fire (RoF) [68]. This was specifically developed for sports aerodynamics, as athletes tend to be in motion, while experiments are done on stationary models. RoF uses HFSB to allow for large scale PIV, it sets up a tent that is filled with the HFSB, and then the athlete (in this case a cyclist) passes through the tent with the light sheet, the use of an actual athlete not only introduces the option for motion, it also eliminates any inaccuracies of the use of a model. The RoF setup used by Spoelstra et al. [64] is shown in figure 3.6. While this setup was specifically designed for sports aerodynamics, it can also be useful for testing the aerodynamics for road going vehicles like cars, trucks etc. on track.

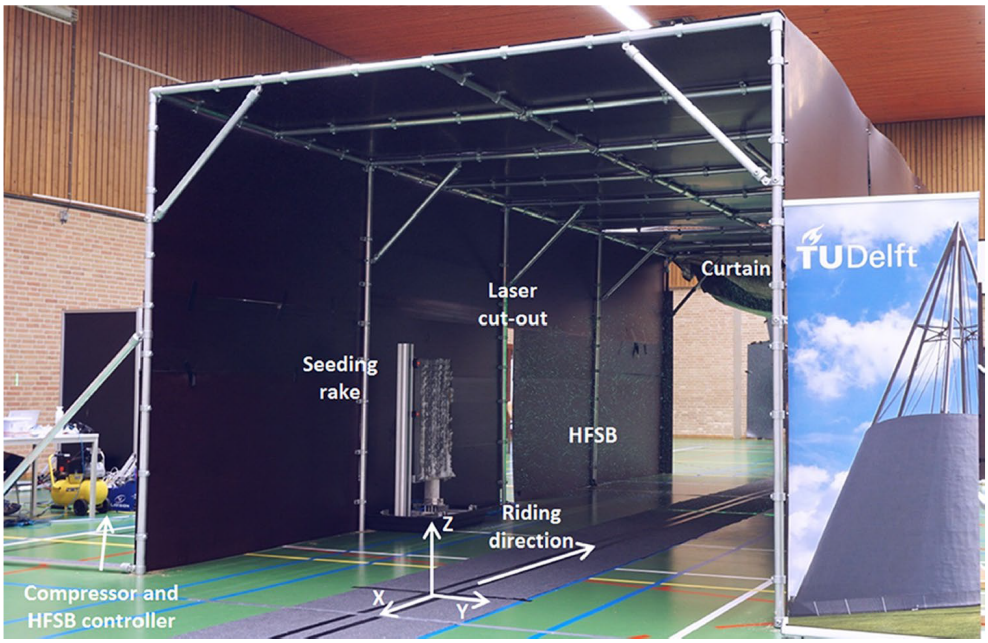

Figure 3.6: Ring of Fire setup as used by [64]

4

Methodology

Two experiments were performed, one preliminary measurement to test the water nozzle and see how well the particles are imaged by the cameras. The second experiment was to use the water droplets for a simple test case to see how well they perform.

4.1. Preliminary Nozzle Tests

The first test is to see how well the droplets are imaged by the cameras, and if PIV can be done successfully with them. The main goal of this test is to get some values for the following parameters:

- Concentration (C)
- Particle production rate ($\dot{N}$)
- Intensity (I)
- Particle diameter (d_p)

The experiment consists of two slightly different setups, the first setup consists of two cameras to quantify the concentration and particle production rate. This requires a full view of the whole production. The second setup uses only one of the cameras with a bigger objective to get a better view of the droplets, this specifically allows for better quantification of the particle diameter. The intensity of the particles will of course differ between both setups, so the first setup will be used to compare the intensity to other particles, in this case Air Filled Soap Bubbles (AFSB). A simplified view of the setup is shown in figure 4.1.

4.1.1. Setup and Hardware

The W-Tunnel at the TU Delft was used for the experiment. The W-Tunnel is an open-jet windtunnel with a choice between a 40x40 cm, 50x50 cm, and a 60x60 cm test section. For this experiment the 40x40 cm test section was chosen. The maximum velocity of the tunnel is 35 m/s, although for this experiment the maximum velocity used was 25 m/s. Depending on flow velocity the minimum achievable turbulence level is around 0.5%. The tunnel has a basic setup: after the plenum and centrifugal fan the flow enters the settling chamber via a diffuser. From this settling chamber it goes through the contraction and through a small nozzle before reaching the exit. The W-tunnel is shown in figure 4.2 with all parts pointed out.

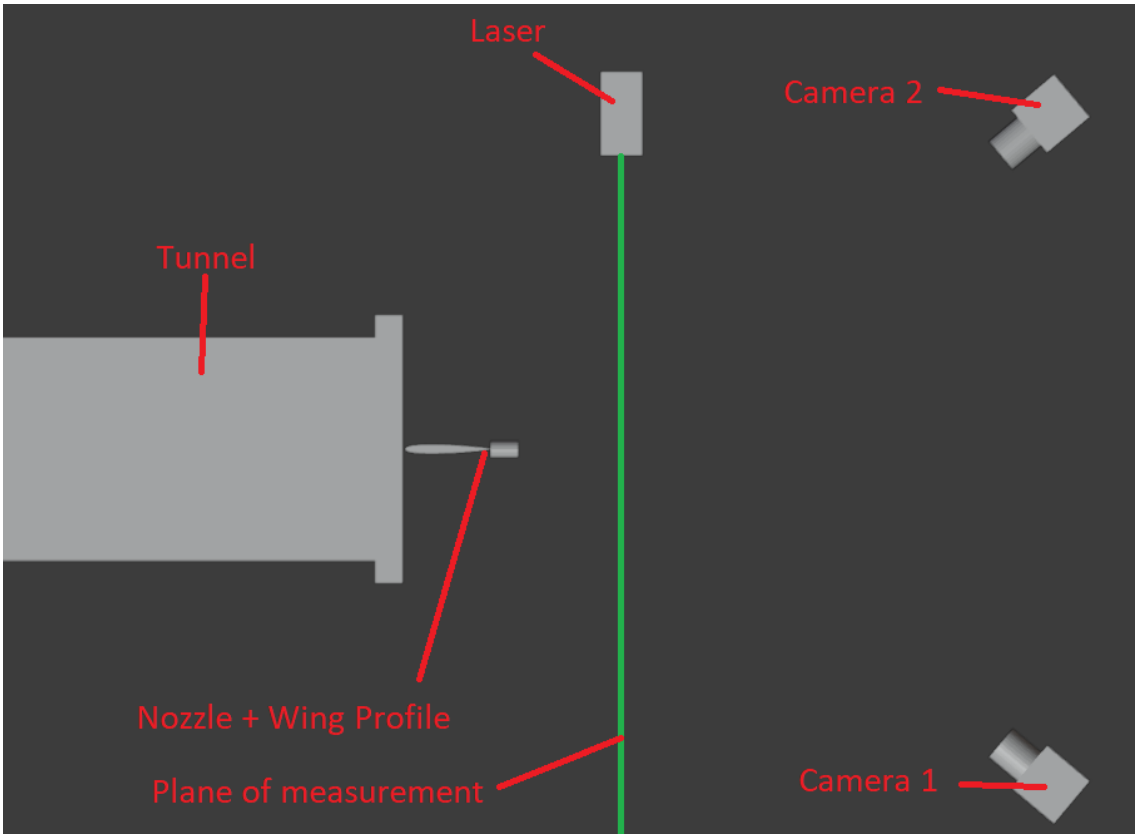

Figure 4.1: Simplified view of the preliminary nozzle experiment setup

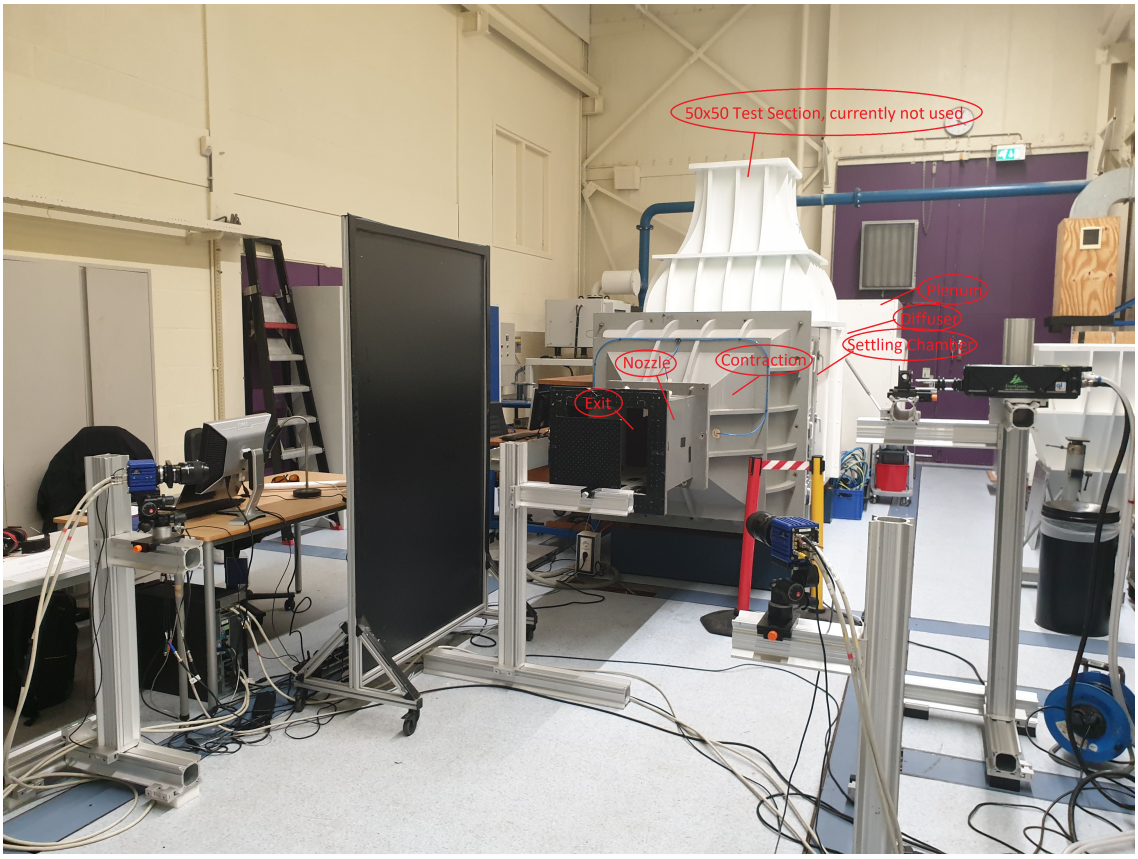

Figure 4.2: The W-tunnel that was used for the experiment.

To produce the water droplets a water nozzle was fitted into the back of a wing profile as can be seen in figure 4.4, with the tubing for the water inside the profile and the switch just outside on the top. The wing profile was then clamped into a custom built clamp and placed just in front of the tunnel exit. To supply the nozzle with water at the right pressure a custom built water supply unit was built (figure 4.3). This is a simple container in which a 2 Liter cup of water is placed. Air is supplied to the container to pressurize, when the exit is opened the water is forced through the exit towards the nozzle. The pressure is controlled at the valve supplying the air to the container. To create the AFSB a single nozzle has been used, this is a nozzle with a single orifice that, contrary to the water nozzle, produces the bubbles one by one. The AFSB nozzle was taped onto the wing profile used for the water nozzle. This arrangement was chosen to best compare the AFSB with the water droplets. One adjustment that had to be made was that the windtunnel had to operate at a much lower velocity of $4m/s$, otherwise the nozzle would be disturbed too much. This would also increase the concentration of bubbles which for a single nozzle would have been possibly too low otherwise.

Figure 4.3: The custom build water supply that was used for the experiment.

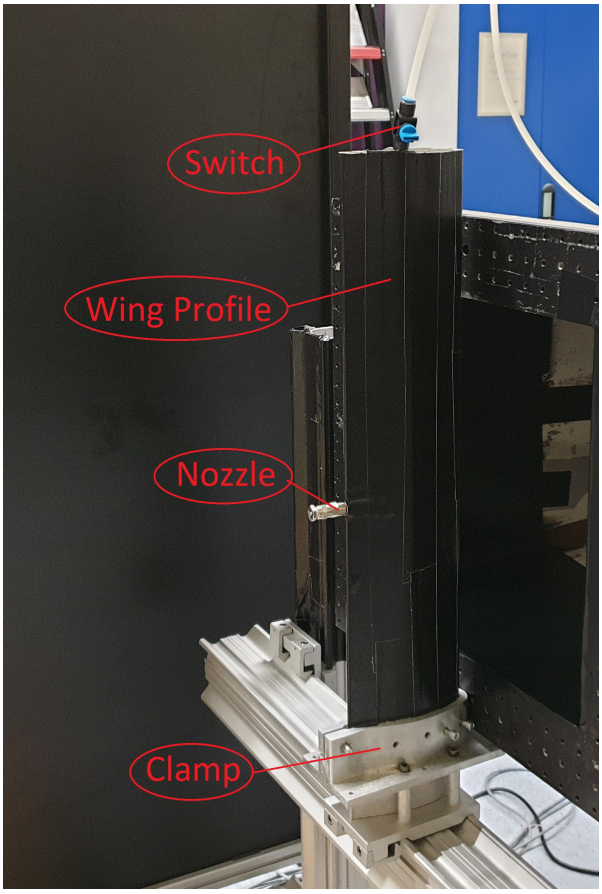

Figure 4.4: A close up of the nozzle setup.

The Quantel Evergreen Laser was used as the light source for this experiment. It is a dual pulsed Nd:YAG laser that produces light pulses of up to $200mJ$ at a repetition rate of $15Hz$, the pulse width is less than $10ns$, the wavelength of the light is $532nm$. To control the dimensions of the laser sheet, various optical lenses were used to expand the laser beams into laser sheets, and two knife edges were placed after these to control the width of the sheet as seen in figure 4.5.

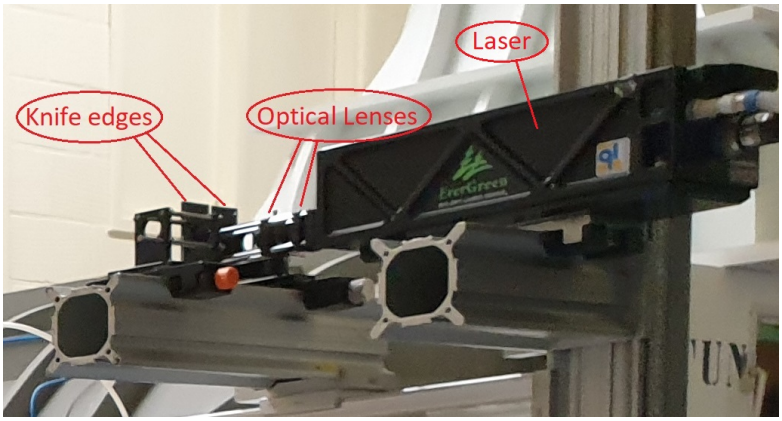

Figure 4.5: The optical lenses and knife edges as used to control the laser sheet

The cameras used for the experiment are the LaVision imager sCMOS. These cameras are double shutter cameras specifically made for PIV experiments that take two images with a $120ns$ minimum

interlacing time. They have a resolution of $2560x2160px$, with a pixel size of $6.5\mu m$. A frame rate of 50 Hz is possible at full resolution, higher frame rates are possible by cropping to lower resolutions.

To control the camera angles, each camera is put on a tripod head, these allow full 3-axis control to the camera.

Each of the cameras has an objective, for this setup two Nikon $105mm$ objectives and one Nikon $180mm$ objective were used. For the first test with both cameras a wide field of view is required to capture the whole production, so the $105mm$ objectives will be used, for the second experiment trying to deduce the particle diameter a smaller field of view is preferred, so the $180mm$ was used. To synchronize all the hardware with the DaVis software that is used, the use of a Programmable Timing Unit (PTU) is required, for this experiment the LaVision PTU-X was used. The full setup with all of the aforementioned hardware can be seen in figure 4.6

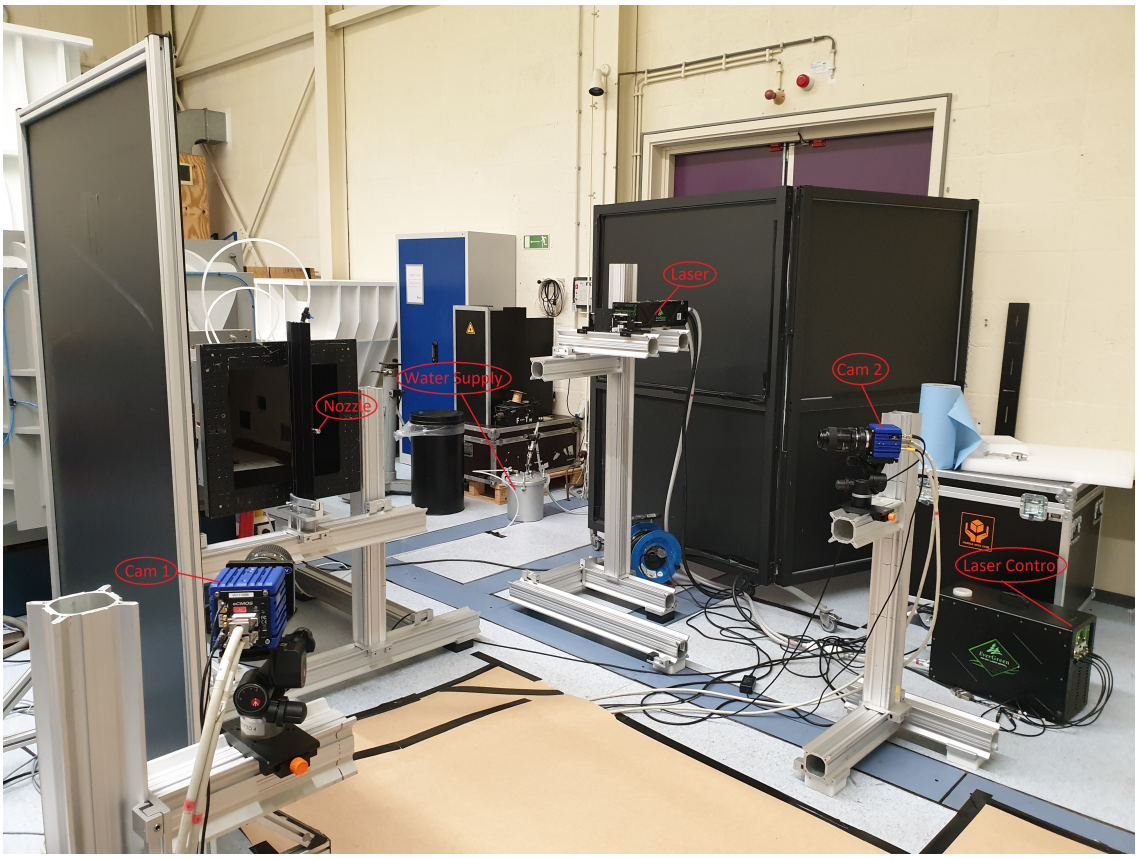

Figure 4.6: The full setup of the experiment.

4.1.2. Experimental Parameters

For the second test covering the particle diameter the resulting particle image diameter can be approximated by the Euclidean sum of the geometric diameter and diffraction limit:

$$d_\tau = \sqrt{d_{geom}^2 + d_{diff}^2} \tag{4.1}$$

where the geometric diameter is defined as:

$$d_{geom} = d_p \cdot M \tag{4.2}$$

and the diffraction minimum diameter limit is defined as:

$$d_{diff} = 2.44 \cdot \lambda \cdot f_{\#} \cdot (1 + M) \tag{4.3}$$

This means the $f_{\#}$ is ideally set as low as possible to ensure d_{geom} has the biggest possible contribution. However the full depth of the laser sheet, which is $2mm$, should be in focus as well. Given the following equation for the depth of view, the minimum $f_{\#}$ needed can be found.

$$d_z = 4.88 \cdot \lambda \cdot f_{\#}^2 \left(\frac{1 + M}{M} \right)^2 \tag{4.4}$$

Where d_z is the depth of view, λ is the wavelength of the light, which is $532nm$, $f_{\#}$ is the F-stop which is the variable that needs to be found, and M is the magnification factor, which for this setup is 0.4. This results in an $f_{\#}$ of 7.93, meaning it will have to be set to 8.

Depending on the velocity the windtunnel is operating at different values for the interval between laser pulses and thus also photos have to be used. The value needed is defined by the fact that ideally the particles should not move more than a quarter of the laser sheet thickness between the two measurements resulting in:

$$\Delta t = \frac{\delta z \cdot 0.25}{V_\infty} \tag{4.5}$$

4.1.3. Analysis

Particle Concentration and production rate

The concentration of particles can be obtained by using equation (4.6)

$$C = \frac{N}{A \cdot \delta z} \tag{4.6}$$

where C is the concentration in $particles/cm^3$, N is the number of particles in the volume. A is the projected surface area in which the particles are present in cm^2, and δz is the laser sheet thickness in cm.

The particle production rate can be calculated with equation (4.7), this equation is only valid if the laser sheet is perpendicular to the flow direction, which for this experiment is true.

$$\dot{N} = \frac{N \cdot V_p}{\delta z} \tag{4.7}$$

Where $\dot{N}$ is the particle production rate in s^{-1}, and V_p is the velocity of the particles in cm/s

Software and Settings

For the processing of the obtained images DaVis Version 8.4.0 was used. First the raw images have a subtract timefilter applied where the minimum intensity over all images is subtracted from each images, this will remove all the static background in the images, raw and filtered images can be seen in figure 4.7a and figure 4.7b respectively. From these images it is clear that the filtered images show almost no background, and the contrast between particles and image background is much higher. After this the 2D particle detection function was used, where an intensity threshold has to be set, this would then allow DaVis to extract the number of particles on each frame. From the filtered images the PIV was also done with the Stereo PIV Multipass function, this was done with a two-pass $128x128$ window, 50% overlap. As a last step the data of all image pairs is then averaged to give a clear indication of the average flowfield.

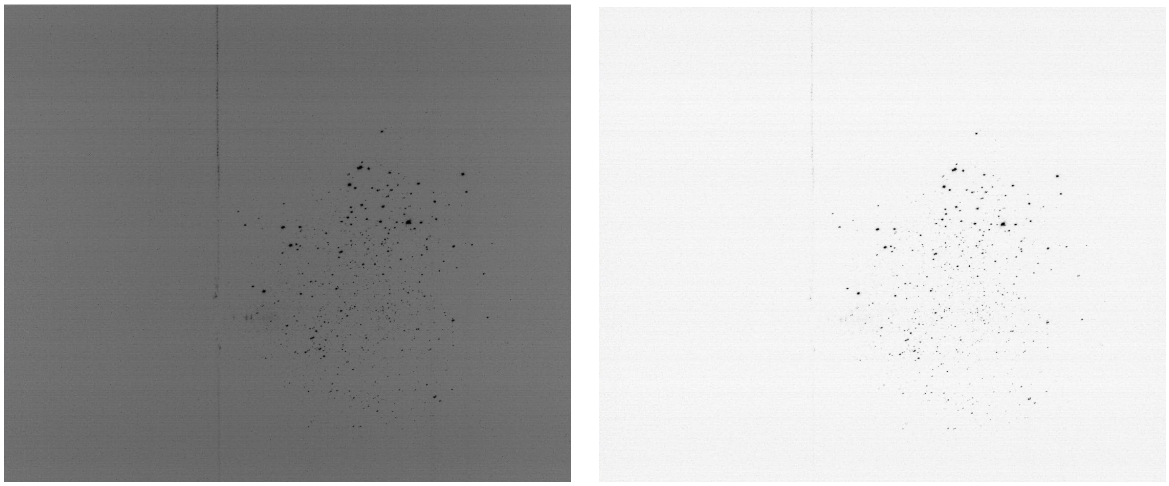

(a) Raw image Water droplets

(b) Filtered image Water Droplets

To determine the best intensity threshold for the particle detection function, some tests were done at different threshold numbers. From the filtered images some clear bands of intensity can be found, these were used to test the threshold. The threshold values tested were $50counts$, $100counts$, and $200counts$.

From these tests it was clear that a threshold of $50counts$ is too low, as there is some background noise that is detected as particles, as well as a lot of the trailing edge of the wing profile the nozzle is attached to. Setting the threshold to $100counts$ removes a lot of the background noise, but still has a decent amount of the trailing edge being detected as particles. Finally setting the threshold to $200counts$ removes all of the background and most of the trailing edge of the wing profile, although it was also seen that some potential particles in the main domain are removed as well, indicating that even higher thresholds are probably going to do more harm then good. In the end the threshold of $200counts$ was chosen, with the main reason being that it removed all of the background noise, furthermore it is likely that the low intensity particles that are removed with this threshold are reflections of particles not in the measurement domain, and therefore are at such a low intensity compared to the other particles.

To determine the diameter of the droplets a Matlab script was used. This script uses the images obtained from the setup with one camera and a $180mm$ objective, which show the glare points more clearly. These glare points are then identified by finding the regional maxima in the image. From these points the closest point within a certain distance and angle limit are found and these two points together form one particle. The initial estimate of the distance is the arithmetic mean diameter the nozzle is certified for which as described earlier is $150\mu m$, with the limits being $\pm 50\%$. A similar limit has been set for the angle between two glare points. This is done to reduce false positives as the angle between glare points is determined by the setup and therefore should not change much during the experiment. Figure 4.8 shows how this angle restriction reduces the amount of false positives. Here the red and blue points are associated with two different particles, which are indicated with a red and blue circle respectively. If there was no restriction on the angle between the glare points, the green circle would have been a potential particle as well. However the angle between the two glare points of this green particle (as indicated by the angle of the line between them) is completely different, and with the angle restriction is therefore discarded. The angle for the glare points was determined to be around 175 degrees with the limits being $\pm 25deg$. The limit for the glare points is a bit stricter as these should not change, and too lenient limits here would give a lot of false positives from nearby particles.

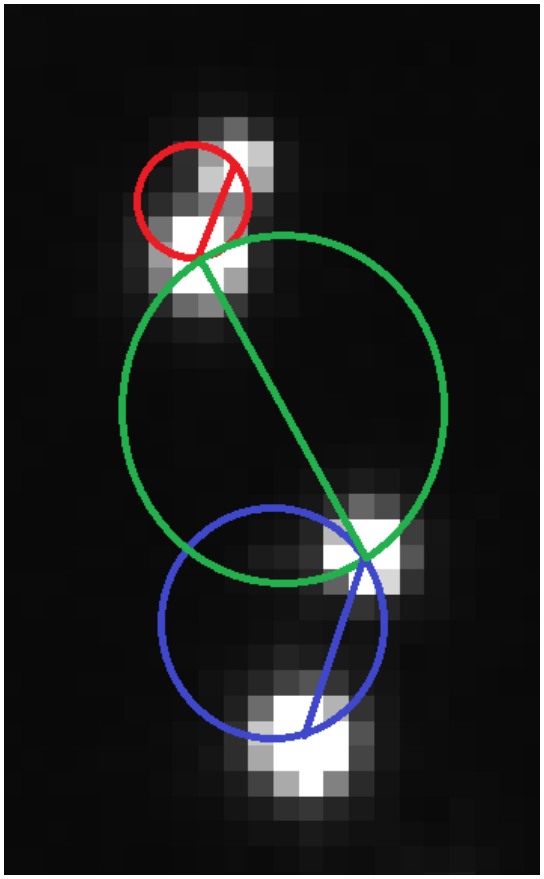

Figure 4.8: Example of how false positives can arise when the angle between glare points is unrestricted. The green circle indicates a false positive droplet created by using a glare point of the red and blue droplet. The lines indicate the angle between the glare points used for each particle.

4.2. Side Mirror Tests

The objective of this second test is to see how well the Shake-the-Box algorithm can track the water droplets, and how the drops interact with an object in the flow. The performance of the water droplets will be compared to HFSB, as they are known to work well as tracer particles for large scale PIV and STB. To achieve this a setup with four cameras has been chosen combined with two LED units. A simplified view of the setup is shown in a 3D view in figure 4.9, and in a side view in figure 4.10.

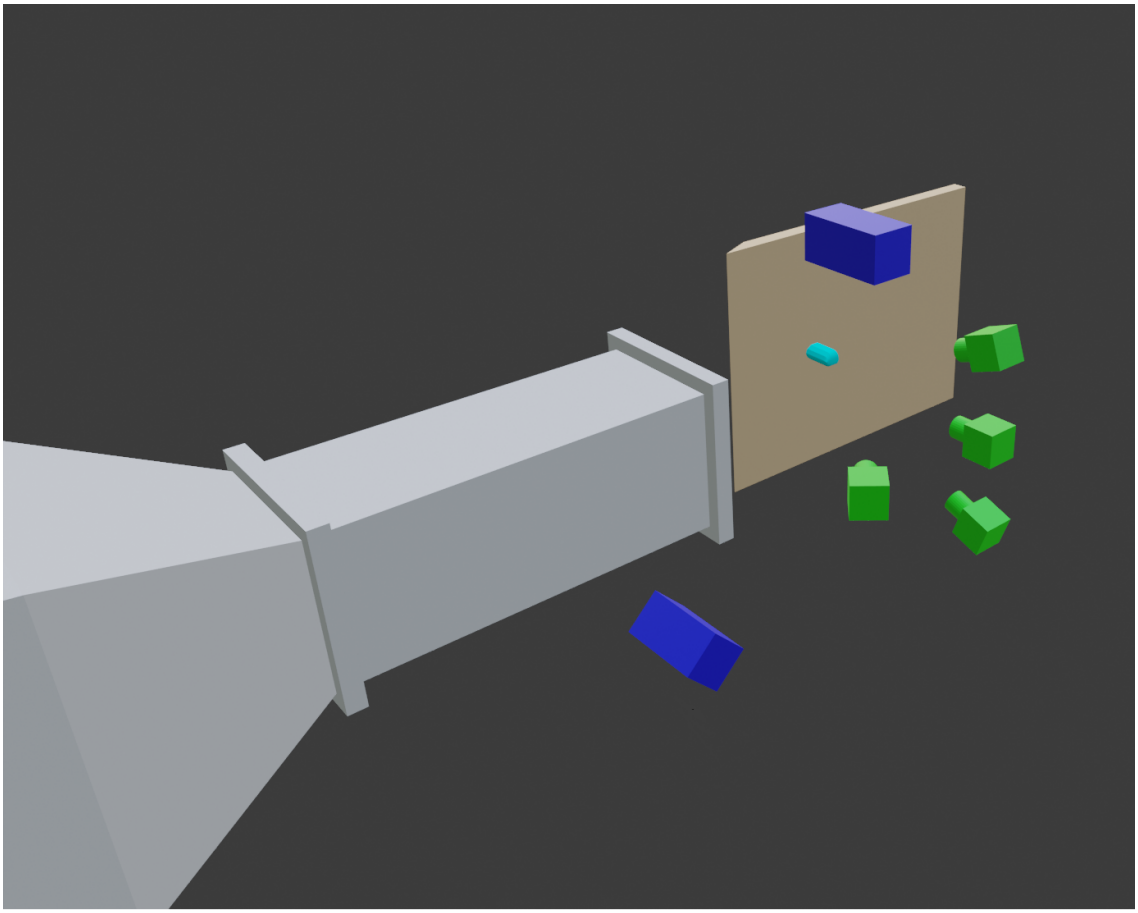

Figure 4.9: Simplified 3D view of the side mirror experiment setup

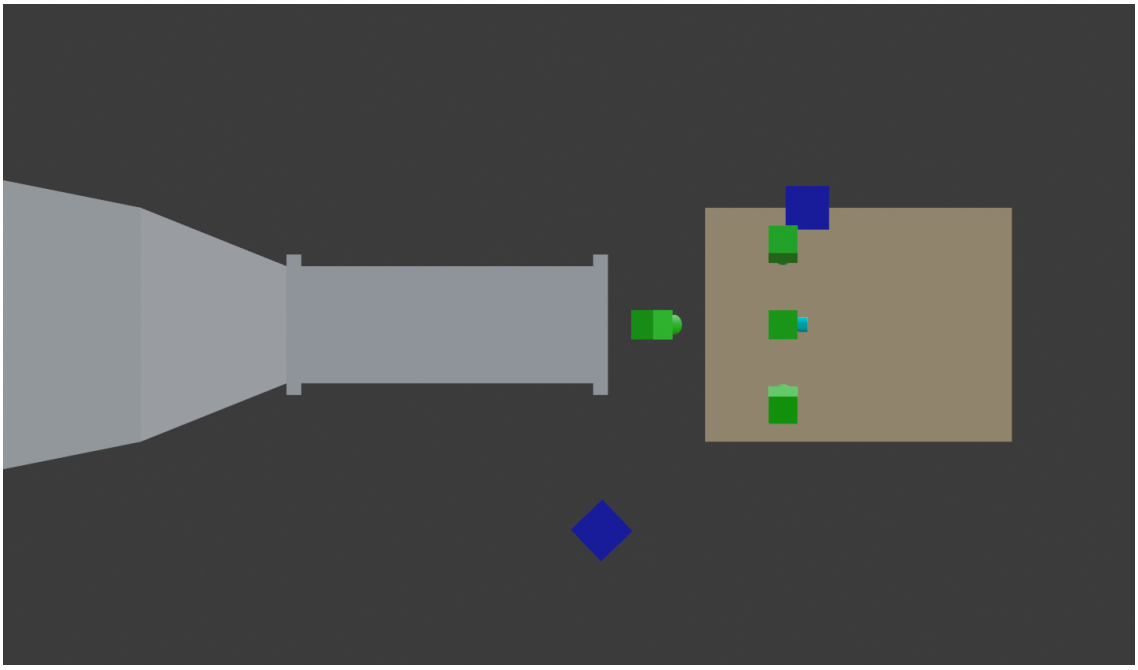

Figure 4.10: Simplified sideview of the side mirror experiment setup

4.2.1. Setup and Hardware

Hardware

For this experiment, the same windtunnel, PTU, Nozzle, and water supply were used as in the first experiment.

Two side mirror models were used for this experiment, first of these is a simple model. This model consists of half cylinder with a quarter sphere on top, both of which have a $5cm$ radius as shown in figure 4.11a. The second model is a $1:2$ scale mirror of a DrivAer model as seen in figure 4.11b, 3D printed and provided by Volkswagen. The DrivAer is a modern generic car model frequently used for aerodynamic tests. To mount the mirrors into the flow a flat plate with a sharp leading edge was used, this represents the flow around a mirror best. The plate, as seen in figure 4.12 with the simple model mounted, is $1m$ long, $0.8m$ high, and $1cm$ thick.

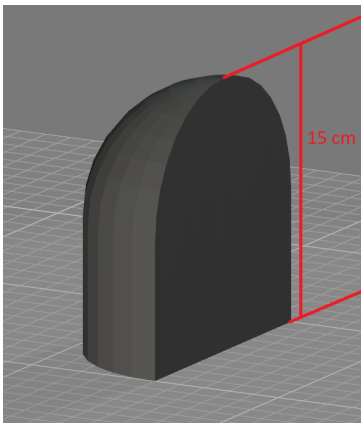

(a) The simple mirror model used.

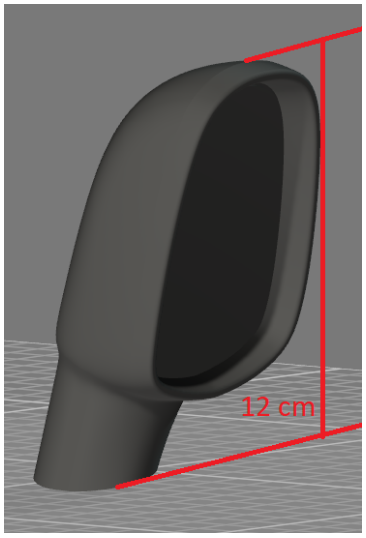

(b) The $1:2$ scale DrivAer mirror model.

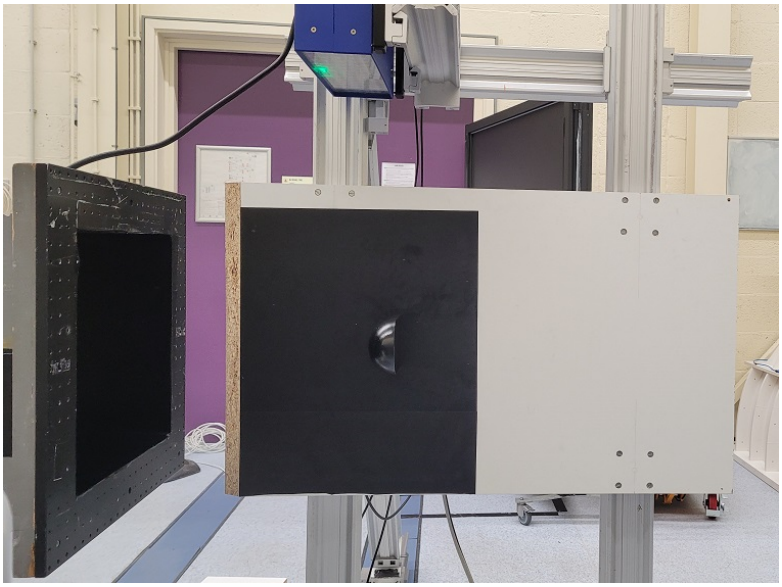

Figure 4.12: The plate used to mount the mirror models.

To generate the HFSB a seeding rake (figure 4.13) was used . This rake consists of 200 nozzles, and can produce up to 30000 Bubbles per second. The average diameter of these bubbles is $400\mu m$ [57].

To supply the rake with the necessary resources, being air, helium, and soap, a custom build Fluid supply unit (FSU) was used. This FSU can regulate the pressure of each of the 3 components, as well as switch to air filled soap bubbles (AFSB) if so desired. Depending on which seeding was needed either the HFSB rake or the wing profile with the water nozzle were mounted in the settling chamber of the windtunnel, for the water nozzle setup the nozzle switch was moved outside of the tunnel so it could be operated from the outside.

Figure 4.13: The HFSB seeding rake used for the experiment.

Two different types of camera were used in this experiment, 3 Photron Fastcam SA 1.1 cameras and 1 Photron Fastcam SA-X2 (provided by Volkswagen). Both of these cameras have a $1024x1024px$ resolution with a $20\mu m$ pixel size. The SA 1.1 cameras have a maximum of $5400fps$ at this resolution, the SA-X2 has a maximum of $12500fps$ at full resolution. Both have the possibility to reach higher fps at lower resolutions, but for this experiment the maximum fps was 5000, so both could operate at maximum resolution. Each of the SA 1.1 cameras used a Nikon $60mm$ Objective, the SA-X2 camera used a Nikon $50mm$ objective due to it's straight position, and therefore slightly smaller distance to the model. Two LaVision LED Flashlight 300 units were used as light sources, these have 72 high power white LED's each, which operate at up to $20kHz$ light pulse trigger. The full setup of the experiment can be seen from two different angles in figures 4.14 and 4.15, a closer look with all the hardware indicated can be seen in figure 4.16.

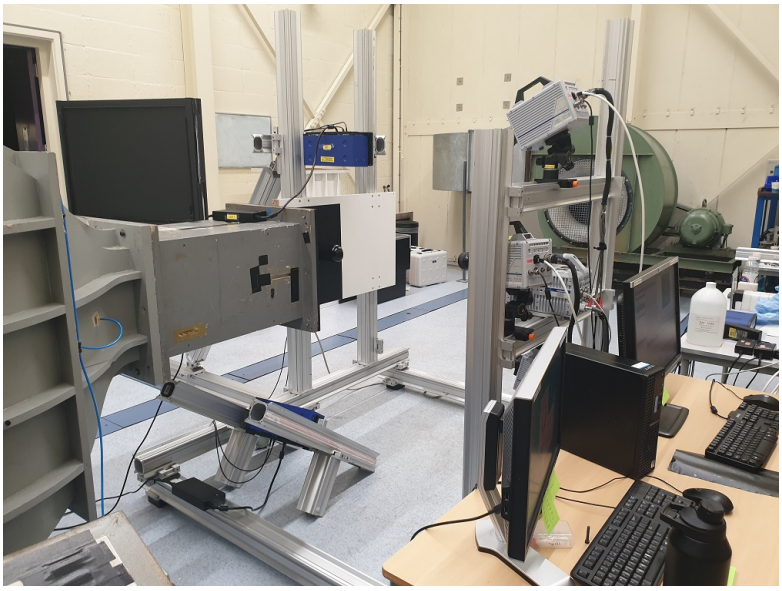

Figure 4.14: The setup of the experiment as viewed from the back.

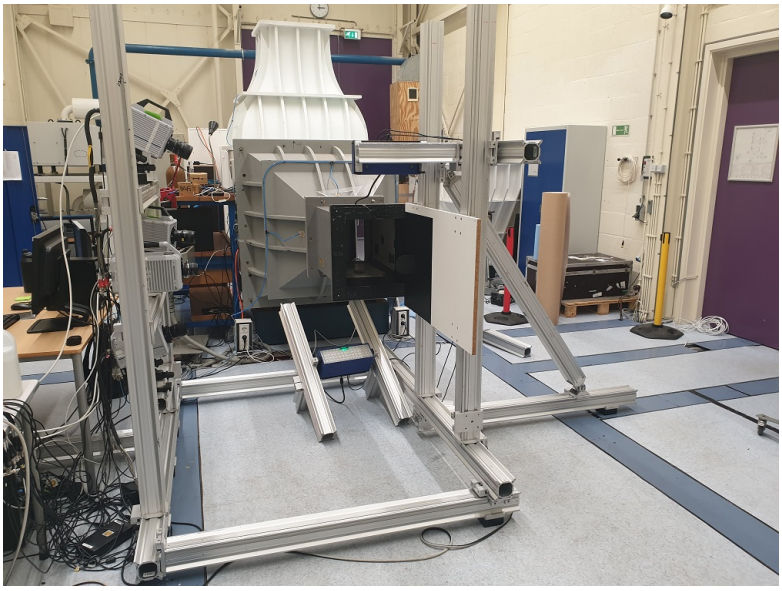

Figure 4.15: The setup of the experiment as viewed from the front.

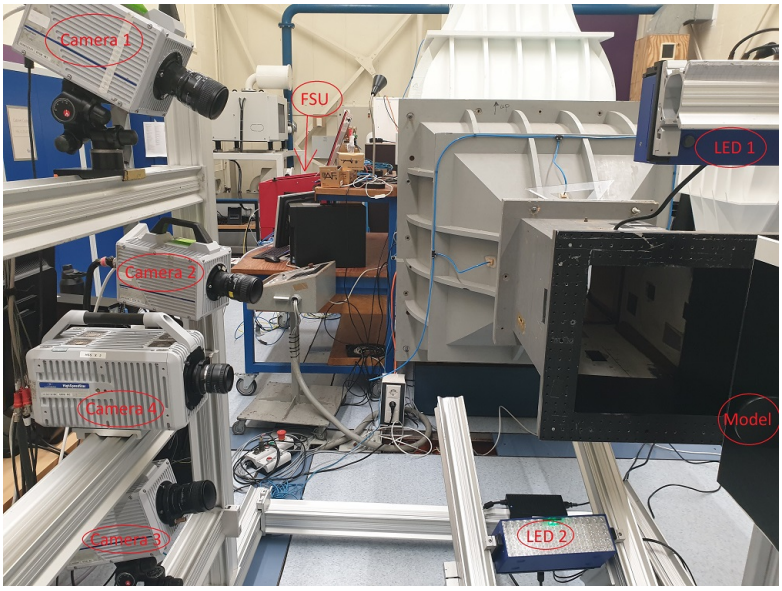

Figure 4.16: The setup of the experiment with annotations.

4.2.2. Experimental Parameters

Measurements were done on two domains, one being the upstream domain covering mostly the uniform flow in front of the mirror and the deceleration area in front of the stagnation point of the mirror model. The other domain being downstream which covered mostly the flow in the wake of the mirror. An indication of both domains is shown in figure 4.17. For the depth of view, equation (4.4) has been used again, this time to have the whole domain in focus. The domain was about $20cm$ in depth, so a $f_\#$ of 16 was used for all cameras. To get good statistics various amounts of images have been gathered per run. For the upstream domain the runs with HFSB had 2000 images, while the ones with water droplets had 3000 images, this was mainly to counteract the lower amount of droplets in each of the images compared to HFSB. For the downstream domain the number of images for both the HFSB and the water droplets was 5000 images, this was due to the increased turbulence behind the model, so more images are needed for proper statistics. Depending on the velocity of the windtunnel different image acquisition rates were used, tests were done at freestream velocities of $10m/s$ and $22m/s$, which used an acquisition frequency of $2kHz$ and $5kHz$ respectively. Both models were tested for both velocities and seeding types (HFSB and Water), each test was also done both for the upstream and downstream domain.

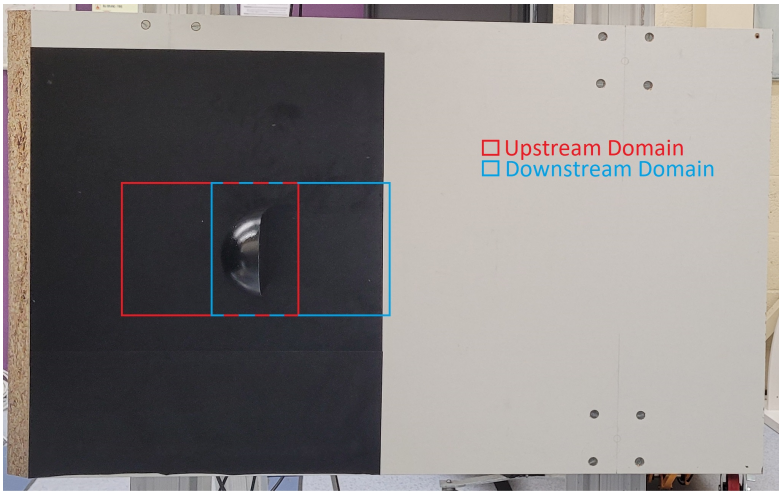

Figure 4.17: Indications of both the upstream and downstream domains, including one of the mirror models.

Software and Settings

For the analysis of the data DaVis 10.2.0 was used. First a Butterworth filter was applied to the raw images, this filter removes non-moving parts of the images, and seems to work a bit better than the subtract minimum filter used in the earlier experiment, the raw and filtered images are shown in figure 4.18a and figure 4.18b respectively. After this the STB function is used to track the particles, lastly to average the data of all frames a binning is done. To visualize all the data from this experiment Paraview 5.11.1 was used.

(a) Raw image Water droplets

(b) Filtered image Water droplets

5

Results

5.1. Spray Characterization

The first spray characterization experiment focused on seeing how well the water droplets are imaged by the cameras. First a comparison with Air Filled Soap Bubbles was made, after which different pressures for the water nozzle were compared.

5.1.1. Comparison with AFSB

Comparing the intensity of AFSB and water droplets is not straightforward to do in a quantitative way. This is due to the fact that for example averaging the counts of an image is also affected by the number of particles compared to background, which is not equal for both cases. It was therefore decided to take the total of all pixels in a small area surrounding a local maximum and average the totals of all particles in an image, the result of which can be seen in figure 5.1. Due to the fact the count of the water particles often reached the sensor limit of 65535 counts there is a bit of a bias here, as the average of the water particles is likely to be higher in actuality. It is however still clear that the average count of the water particles is higher by roughly $25000 counts$, indicating they are at least twice as bright as the AFSB.

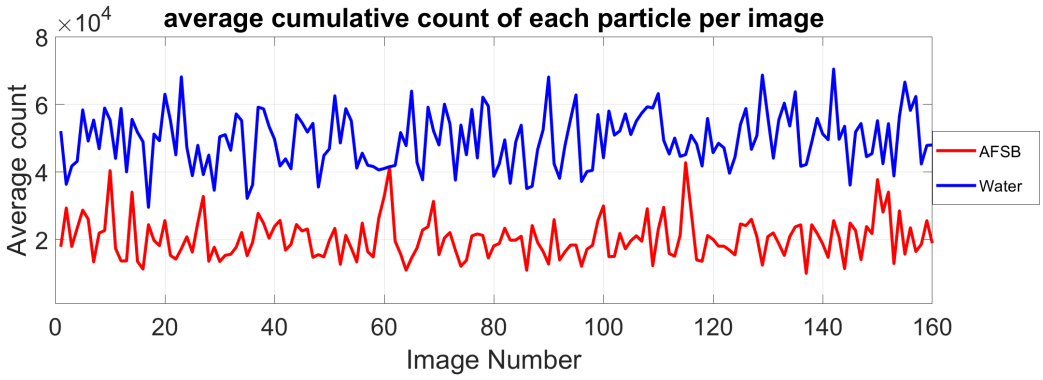

Figure 5.1: Average cumulative count of each particle for each image

Comparing the number of particles for both seeding types is fairly straightforward, as DaVis has a build-in function to do so. The number of particles of each image, plotted as a histogram can be seen in figure 5.2. From this figure it can be seen that the amount of particles is roughly four to five times as high for the water nozzle. It can also be seen that the spread of the amount of water droplets is a bit higher in absolute terms (± 75 for water vs ± 30 for AFSB), but compared to the average it is similar to that of the AFSB ($\pm 35\%$ for water vs $\pm 50\%$ for AFSB) . This means the water droplets produce a similarly constant stream of particles as AFSB, meaning it should be sufficient for PIV.

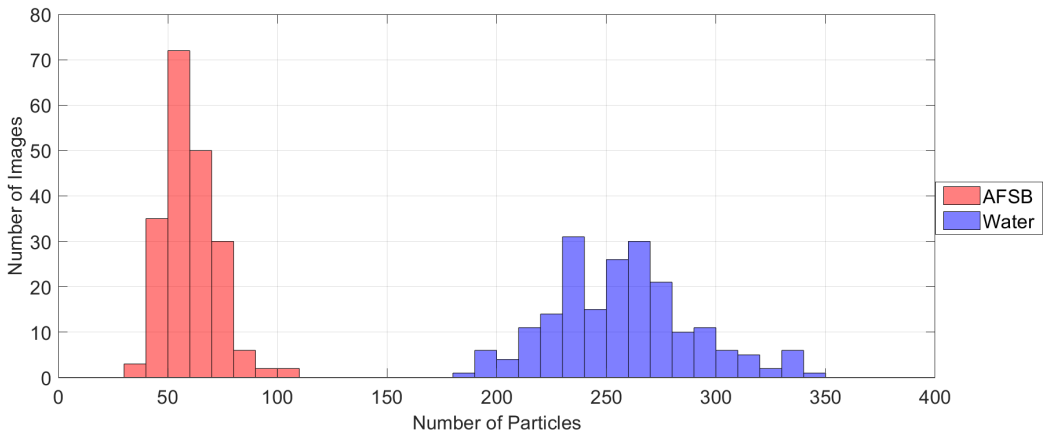

Figure 5.2: Average number of particles per image as a function of Pressure

The resulting average velocity fields obtained from the PIV done are shown in figure 5.3a for AFBS and in figure 5.3b for the water droplets. As described in chapter 4, the AFSB test was done with a much lower freestream velocity ($4m/s$ instead of $20m/s$. This lower velocity allows for the bubbles to spread relatively much. For the water nozzle it is the other way around, the nozzle produced droplets in a cone, but due to the velocity of the flow surrounding it, it cannot expand as much. The first major observation is that in both cases the particles have a velocity significantly lower than that of the freestream they were in. The most likely cause of this is the fact that the nozzles were mounted on a wing profile, this means the particles are released in the wake produced by the wing profile, resulting in them experiencing a lower flow velocity than that of the freestream. To ensure both velocity fields show relevant data the data has been re-scaled to different velocities for both cases. The end result is that the size of both jets is of the same order size at the measurement domain. Both also show similar flow patterns, with a higher velocity in the center, which tapers off the further from the center the particles are. One difference that can be observed is that the water droplets seem to have a bit of noise to the left of the jet, this is most likely caused by reflections of the water droplets, which tend to be stronger than for AFSB. Lastly it can be seen that the PIV done on the water droplets gives similar results to that of AFSB, and are therefore performing well as tracer particles.

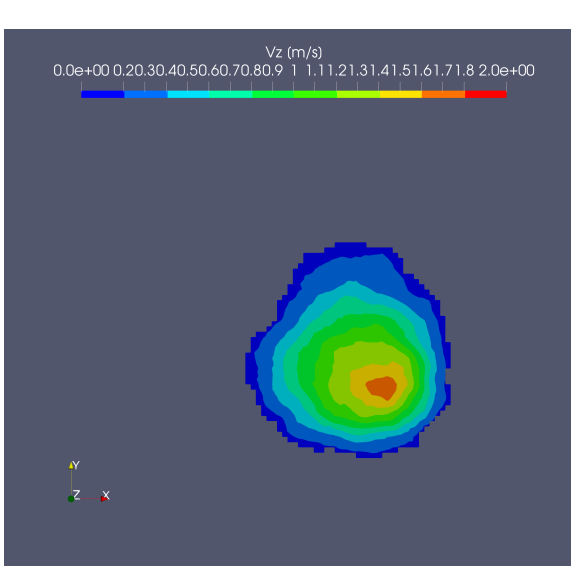

(a) Average flow velocity obtained with PIV for the AFSB

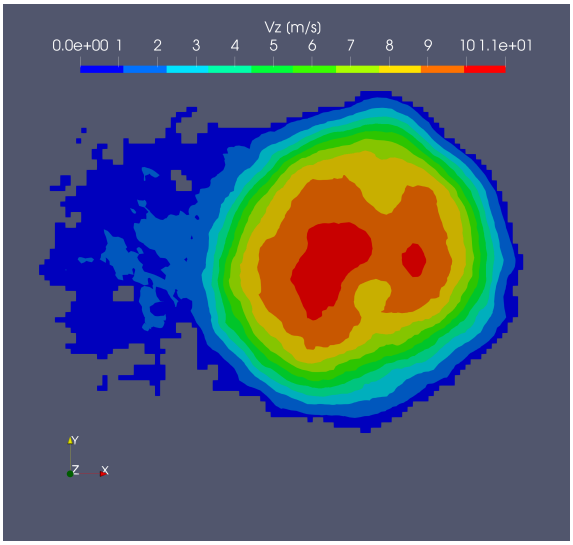

(b) Average flow velocity obtained with PIV for the Water droplets at 3 bar

Figure 5.3: Average flow velocity obtained with PIV for AFSB (a) and water droplets at 3 bar (b)

To get the concentration of particles, equation (4.6) was used as described in chapter 4. To obtain the number of particles present, the average over all images is taken (N_{avg}). The projected surface area in which the particles are present is calculated by taking the diameter of the jet, as can be seen in the PIV results, and then calculating the circular area associated with this diameter. This assumes the jet is a perfect circle at the measurement plane, which by looking at the PIV results seems to be a good approximation. To get the production rate of the particles equation (4.7) was used as described in chapter 4. The particle velocity is obtained by taking the average velocity of the particles from the average flowfield. The final results of both the concentration and production rate calculations is shown in table 5.1, this includes all relevant parameters for the calculations. The water pressure used for this comparison was 3 bar as the nozzle was rated at that pressure. From this table it can be seen that while the water nozzle produces a lot more droplets, the fact that the droplets are spread out over a wider area, and the operating velocity of the windtunnel being higher allows for the concentration of particles to differ only by roughly 10%.

Seeding	N_{avg} [-]	Diameter of seeded streamtube [cm]	avg. Particle Velocity [cm/s]	A [cm^2]	$\dot{N}$ [$particles/s$]	C [$particles/cm^3$]
AFSB	30	7.5	78.7	44.6	2353	0.671
Water	98	12.4	698	122	89700	1.06

Table 5.1: Table showing the Concentration and Particle production rate for both the AFSB and Water droplets (3 bar pressure). Includes the relevant parameters used for the calculations.

5.1.2. Effect of Pressure

To see the effect of the different pressures on the amount of particles produced the distribution of particles per images for all pressures is plotted in figure 5.4, these are all done at a free steam-velocity of $20m/s$. From this it can be seen that as the pressure increases the number of particles also goes up. Notably the difference between 2 bar and 2.5 bar is small compared to the jumps between other pressures. Some possible causes of this include a temporary blockage in the nozzle during measurement, or the water running low at the end of measurement, normally the nozzle would stutter when water was running out, but it is possible that before that point arrives the nozzle already produces fewer droplets.

Comparing the PIV results of the 2 bar test case (figure 5.5a) and of the 3 bar test case (figure 5.5b) show that a higher pressure causes higher velocities in the center of the jet as well as a larger jet diameter. This is as to be expected as the higher pressure causes the water to come out with more force behind it, as a result the exit velocity of the droplets is higher. This in turn causes the droplets to get further from the nozzle exit before entering the measurement plane.

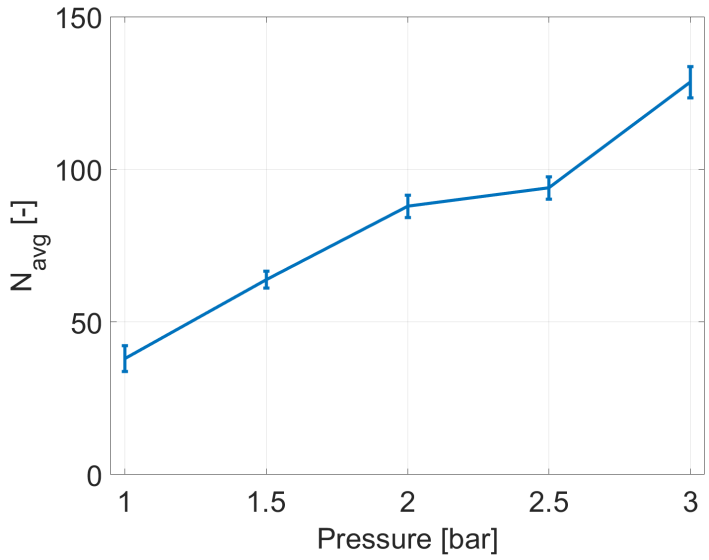

Figure 5.4: Number of particles for each image

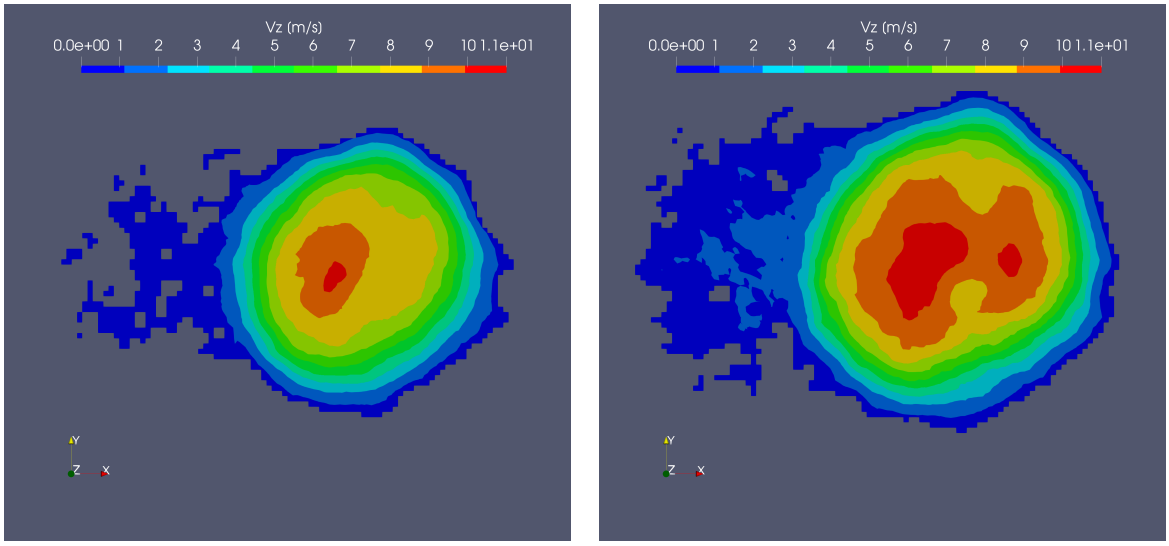

(a) Average flow velocity obtained with PIV for water droplets at a pressure of 2 bar

(b) Average flow velocity obtained with PIV for water droplets at a pressure of 3 bar

Figure 5.5: Average flow velocity obtained with PIV for water droplets at a pressure of 2 bar (a) and 3 bar (b)

Plotting the average number of particles and particle production rate is done in figure 5.6a and figure 5.6b respectively, these show that the average number of particles increases fairly linearly with the increase in pressure. A similar behaviour can be seen for the particle production rate, indicating that the average particle velocity does not change too much compared to the number of particles, which would otherwise resulted in a more different shape of the graph. This is as expected as the main driver for the particle velocity is the free-stream velocity the water droplets are adapting to, which was unchanged. The seeded streamtube diameter and concentration are plotted as a function of pressure in figure 5.7a and figure 5.7b respectively. From these it can be seen that the diameter of the seeded streamtube increases quite sharply at first, after which it increases in a more linear fashion, similarly the concentration shows a sharp decrease in the first step after which it is quite stable. This most likely is caused by droplets not being forced out of the nozzle, but slowly dripping out due to the low pressure. As a result the droplets do not move far from the nozzle resulting in a high concentration of particles in

a small area. Therefore it seems that 1 bar of pressure might be too low of a pressure for this nozzle, to check this the PIV results of this run are shown in figure 5.8.

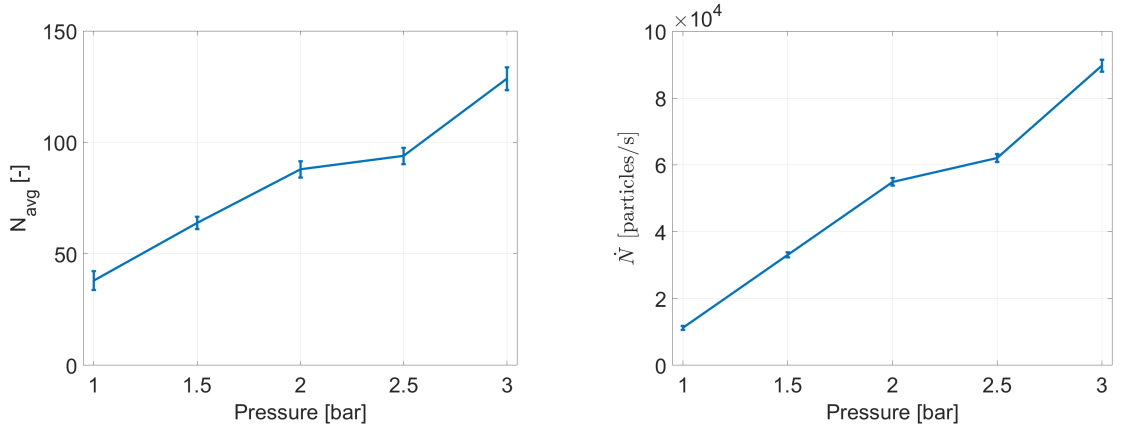

(a) Average Number of particles as a function of Pressure at a free-stream velocity of $20m/s$

(b) Particle production rate as a function of Pressure at a free-stream velocity of $20m/s$

Figure 5.6: Average number of particles, and particle production rate as a function of pressure.

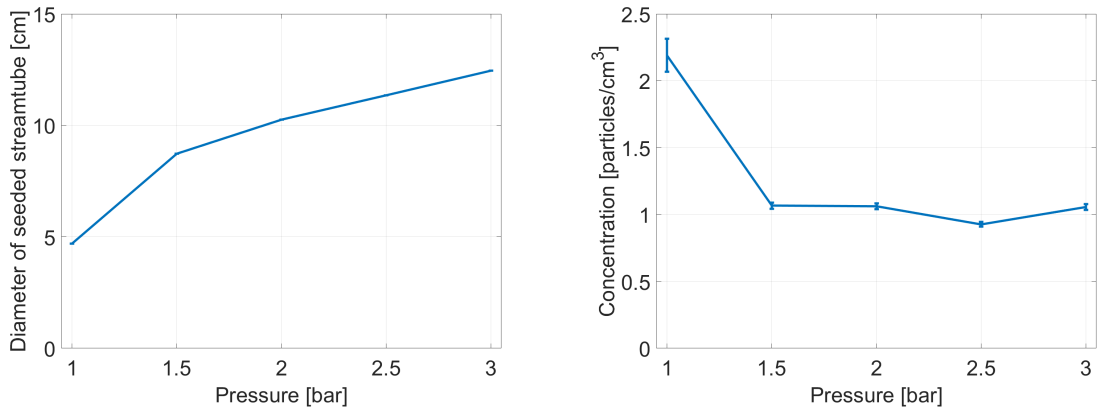

(a) Diameter of the seeded streamtube as a function of Pressure at a free-stream velocity of $20m/s$

(b) Concentration as a function of Pressure at a free-stream velocity of $20m/s$

Figure 5.7: Diameter of seeded streamtube, and concentration as a function of pressure.

From here it can be seen that there is not a neat circular shape as seen in for example figure 5.5b, but more of an oval shape. Furthermore the velocity is a lot lower compared to the other cases. As mentioned earlier, this is most likely caused by the water droplets not being forced out of the nozzle enough and slowly dripping out, coalescing at the exit into bigger drops instead of neat droplets. Table 5.3 shows the same results in a numerical format. Looking specifically at the diameter of the seeded streamtube (and by extension the concentration) the pressure of 1 bar is a clear outlier, indicating the nozzle is operating at too low of a pressure. For the 1.5 bar pressure most values do fall in line with ratios between the other pressures, with the one exception being the particle velocity. The most likely explanation for this discrepancy is the fact that the larger droplets present at 1.5 bar are still adapting to the flow velocity at the point of measuring. Equation (5.1) shows the particle time response which is defined as the time for a particle to adapt to 63% of a change of velocity in the flow. Here ρ_p is the particle density, and μ is the dynamic viscosity of the flow medium. From this the various time response values for the different particles can be calculated. For the AFSB this requires the density to be calculated. To do so first the diameter of the bubbles needs to be found, which was found to be $246\mu m$. Given this diameter and assuming that the HFSB is exactly neutrally buoyant (and therefore

has the same density as air) the soap film thickness can be found to be $83nm$, which seems accurate given the soap film thickness in literature was found to be $100nm$ [15]. From the calculated diameter the volume (and therefore mass) of the air inside the AFSB can be found. Combining this mass with the mass of the soap film gives then the mass which can be translated to the density of the AFSB, which was found to equal $2.283kg/m^3$. The calculated time responses can then be calculated, the results of which are shown in table 5.2. The diameter of the water droplets was taken to be $0.214mm$ and $0.226mm$ as shown in figure 5.9 represents the particle diameter at 2 and 1.5 bar respectively. For the HFSB it was assumed that they have a slightly higher density than that of air ($1.325kg/m^3$), this is due to the fact that they are not perfectly buoyant, and from literature it was found that they do show a time response of $10-30\mu m$ [57]. In reality there are factors that have been neglected to reach equation (5.1), which would come into play if the particle density equals that of the surrounding fluid, but as this is just for a order of magnitude comparison this assumption will suffice. From table 5.2 it can be seen that the time response of the AFSB is an order of magnitude larger than that of HFSB ($18.7\mu m$ vs $198\mu m$), the water droplets show a time response that are another 3 orders of magnitude larger ($141-157ms$). Comparing the two different water droplets shows that the increase in particle diameter between the two pressures increases the time response by about 10%. This increase in time response of 0.016 seconds might seem small, but given the windtunnel was operating at $20m/s$ this results in a difference of $0.2m$. As the measurements were performed fairly close to the nozzle exit, this can explain why the particle velocity of the particles at 1.5 bar is relatively low compared to the higher pressures.

Particle Type	Diameter [mm]	Density [kg/m^3]	τ_p [s]
HFSB	0.246	1.225	1.87 $\cdot 10^{-5}$
AFSB	0.246	2.283	1.98 $\cdot 10^{-4}$
Water	0.210	1000	0.141
Water	0.226	1000	0.157

Table 5.2: Response times calculated for the different types of particles

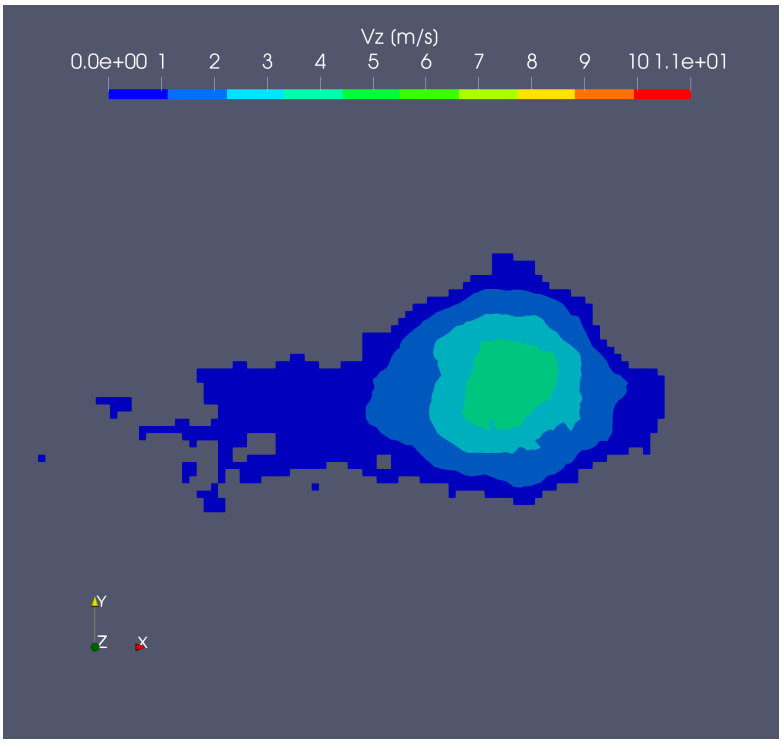

Figure 5.8: Average flow velocity obtained with PIV for water droplets at a pressure of 1 bar

Pressure [bar]	N_avg [-]	Diameter of seeded streamtube [cm]	Particle Velocity [m/s]	A [cm^2]	$\dot{N}$ [$particles/s$]	C [$particles/cm^3$]
1	38	4.70	2.95	17.3	11206	2.19
1.5	64	8.74	5.17	59.9	33053	1.07
2	88	10.2	6.25	82.7	54936	1.06
2.5	94	11.3	6.61	101	62033	0.927
3	129	12.4	6.98	122	89700	1.06

Table 5.3: Table showing the Concentration and Particle production rate for different pressures. Includes the relevant parameters used for the calculations.

$$\tau_p = d_p^2 \frac{\rho_p}{18\mu} \tag{5.1}$$

Finally the particle diameter as a function of pressure is plotted in figure 5.9. From this it can be seen that as one would expect the particle diameter gets smaller as the pressure is increased. The Arithmetic mean diameter obtained from this test is $0.210mm$ which is significantly higher than the nozzle is rated at. There can be multiple reasons for this, first and foremost the pressure for the test was measured before entering the water supply, and therefore fairly far from the nozzle itself. As a result some pressure losses are likely to have occurred, this will most likely not have been the case during the certification of the nozzle, therefore it is reasonable to assume the particles in the test should be a bit larger than would be assumed from the nozzle certification. Looking at figure 5.9 however shows that there would have to be large pressure loss to fully explain the difference in particle diameter. As described in chapter 4, the particle diameter is calculated by identifying regional maximums in the images and assuming these are one of the glare points. For smaller particles it is possible that the glare points are connected or even overlap, as a result the other glare point is not found and the particle is discarded. This means that there is a bias to larger particles, which in combination with the pressure losses could explain the difference with the certified particle diameter.

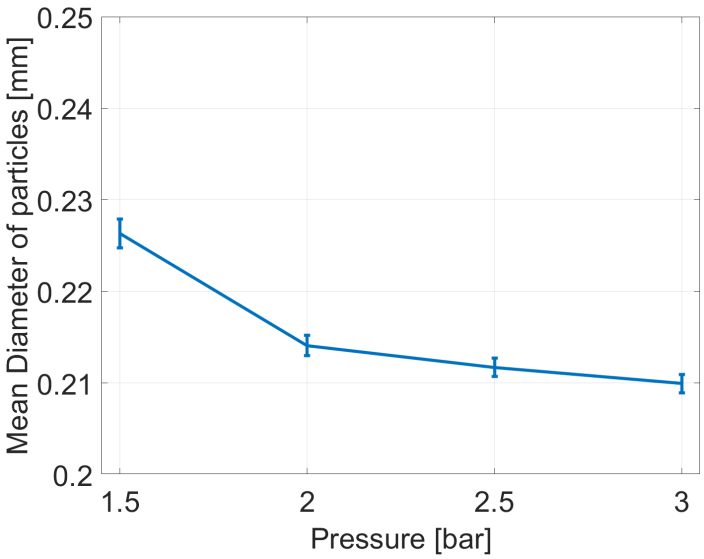

Figure 5.9: Particle diameter as a function of pressure.

5.2. Side Mirror flow results

The side mirror experiment focused on the behaviour of the water droplets in a flow around a side mirror. A comparison is made with HFSB, different mirror models, and at different freestream velocities.

5.2.1. Flow Visualization

The flow around the mirror can be described by a few distinct areas, which share some similarities with the flow around a cylinder. First off there is a stagnation region in front of the mirror where the flow decelerates as it approaches the stagnation point. The next distinct region is those on top and bottom of the mirror, here the flow accelerates as it flows around the mirrors contours. As the flow separates near the top and bottom two shear layers emerge. Between these shear layers is a wake region with recirculating flow. Further downstream, behind the recirculation area the flow reattaches to itself before it steadily accelerates back to the freestream.

To give a better visual of the flow the results for HFSB at 22 m/s and 10 m/s are shown in this section. The mean flow in the XY-plane is shown in figure 5.10, the mean flow in the XZ-plane is shown in figure 5.11. Lastly an isosurface of $u = 0m/s$ is shown in figure 5.13 with some streamlines. From these images it is clear that the normalized flow of the two cases are very similar. The only difference being the fact that the flow for the 22 m/s case seems to flow around the mirror more, indicating later separation. The width of the wake at the end of the measurement domain is also slightly smaller for the 22 m/s case. While hard to see in these figures, showing the velocity profile at 170 mm behind the mirror, as done in figure 5.12 shows the difference more clearly. The velocity profile shows that the wake for the 22 m/s flow is indeed slightly smaller, indicating earlier reattachment. From the isosurface comparison one notable difference is the fact that the isosurface of 0 m/s seems to be larger for the flow at 10 m/s, indicating that the re-circulation area behind the mirror is larger for this flow, confirming the fact that the reattachment of the flow is at a later point compared to the 22 m/s flow.

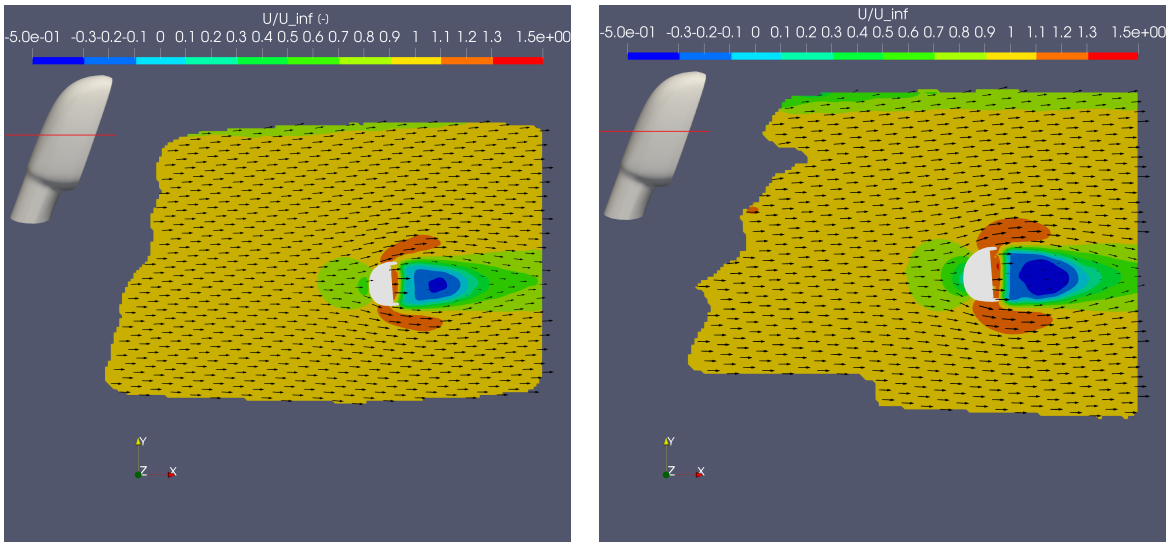

(a) Mean flow in the XY-plane at a freestream velocity of 10 m/s.**(b)** Mean flow in the XY-plane at a freestream velocity of 22 m/s.

Figure 5.10: Mean flow in the XY-plane at a freestream velocity of 10 (a) and 22 (b) m/s

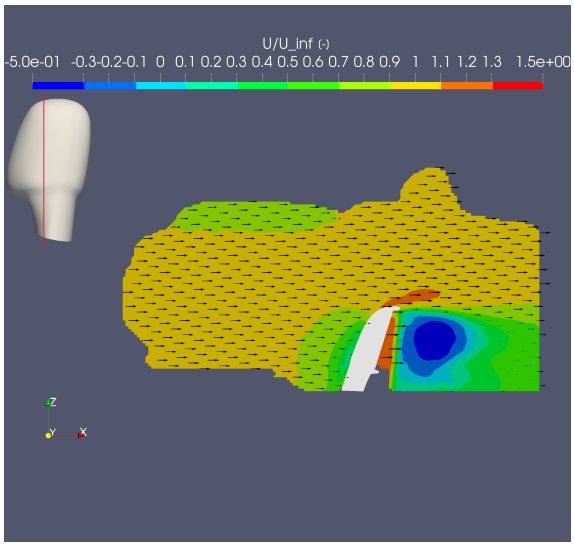

(a) Mean flow in the XZ-plane at a freestream velocity of 10 m/s.

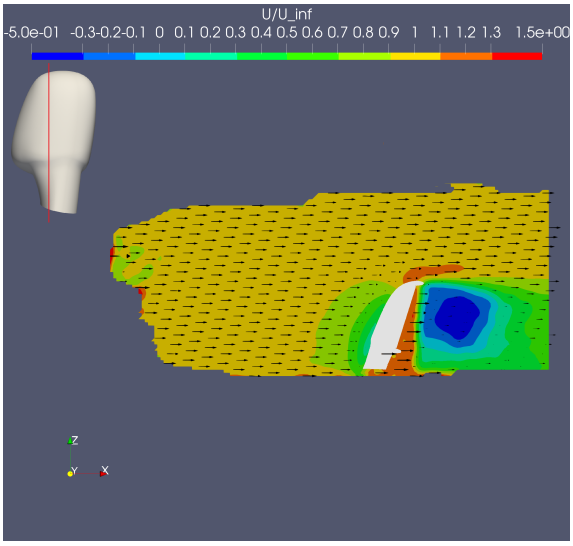

(b) Mean flow in the XZ-plane at a freestream velocity of 22 m/s.

Figure 5.11: Mean flow in the XZ-plane at a freestream velocity of 10 (a) and 22 (b) m/s

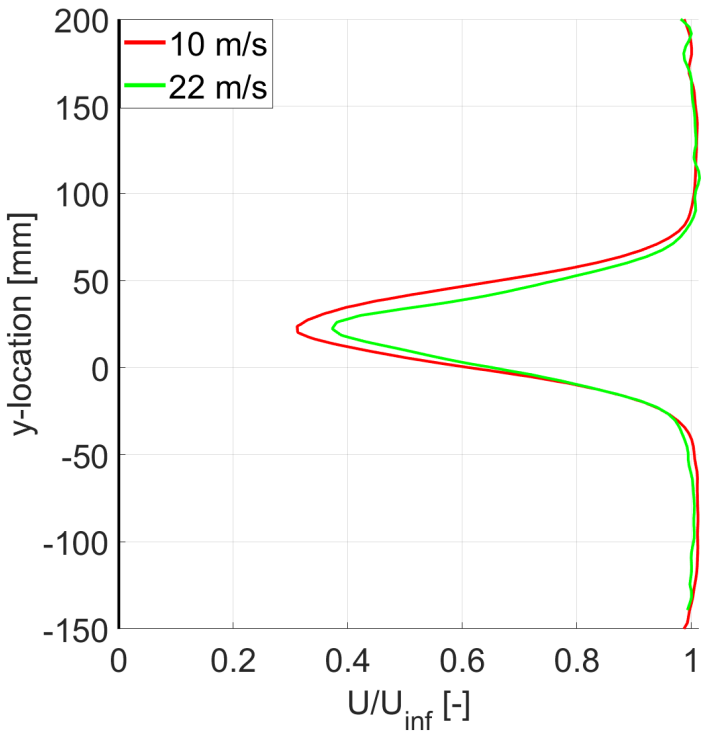

Figure 5.12: Velocity profile for both 10 and 22 m/s cases at 170 mm behind the mirror model.

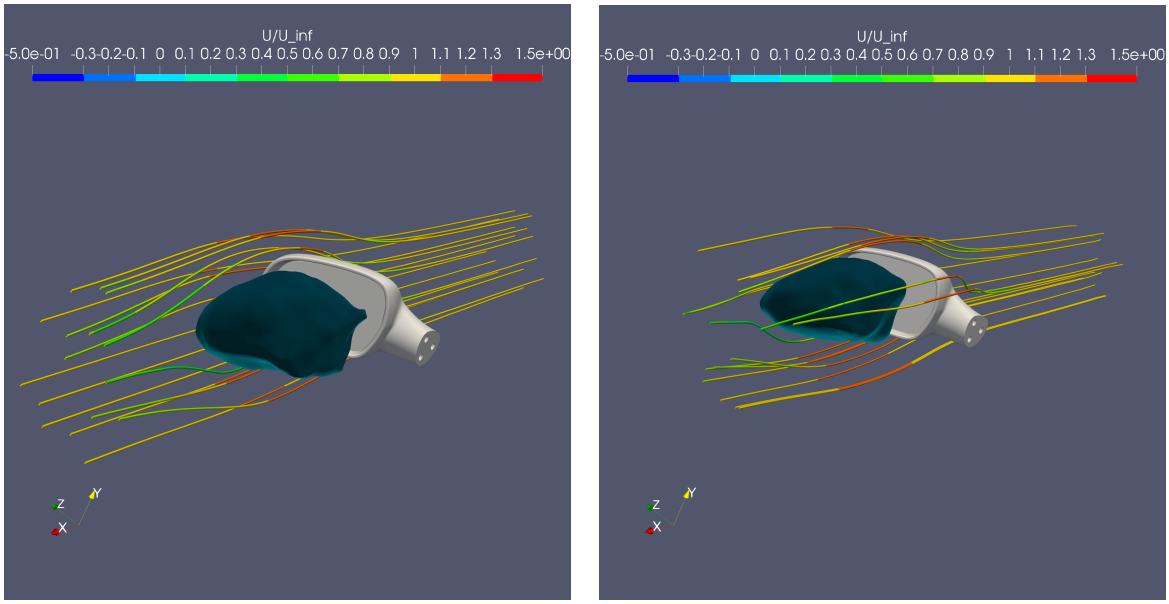

(a) Iso-surface of $u = 0m/s$ and streamlines of the flow at a freestream velocity of 10 m/s..

(b) Iso-surface of $u = 0m/s$ and streamlines of the flow at a freestream velocity of 22 m/s..

Figure 5.13: Iso-surface of $u = 0m/s$ at a freestream velocity of 10 (a) and 22 (b) m/s

To give an insight into the fluctuations and reliability of data in certain areas the standard deviation of the normalized velocity in x-direction is shown in figure 5.14. From these it can be seen that there are a couple of areas where the standard deviation is higher. First of all there is the wake that has a slightly increased standard deviation, which is as expected due to the dynamic flow present there. Since the velocities in this area are rather small the fluctuations tend to be small as well, causing only a light increase in standard deviation here. Furthermore the area directly behind the model shows a significantly higher standard deviation, this is easily explained by the fact that there are little to no particles directly near the mirrors surface, as there is also limited flow here. Lastly there are regions emanating from the tips of the mirror that also show a high standard deviation. Looking at the XY-plane specifically these locations are exactly where the shear layers are present, since these shear layers tend to wobble a bit there are extreme velocity fluctuations here as in these regions the flow fluctuates between the high velocity free stream air and the much lower velocity wake flow.

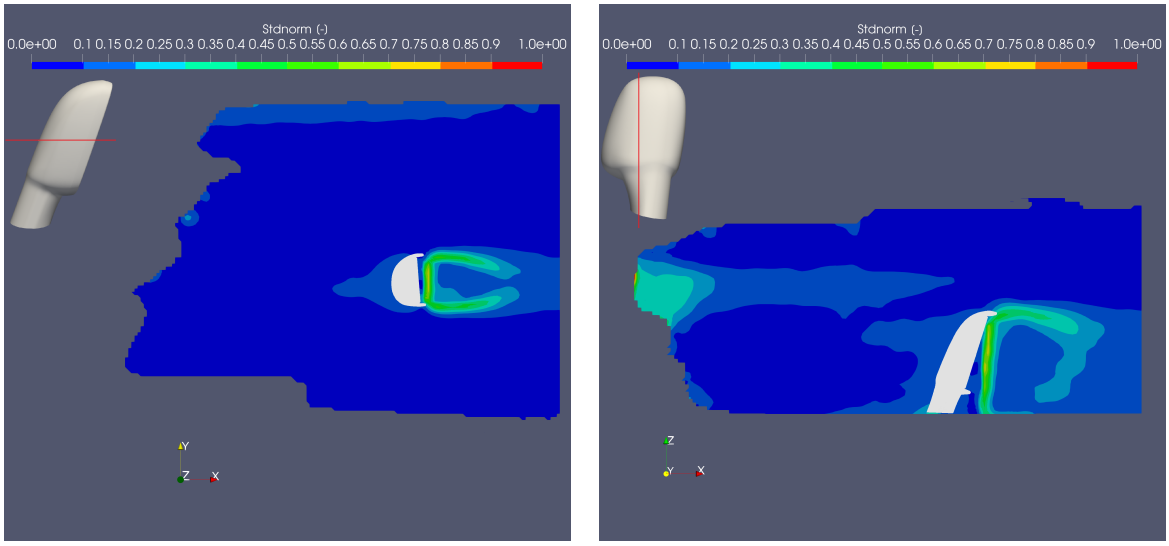

(a) Standard deviation of the normalized velocity in x-direction for HFSB in the XY-plane at a freestream velocity of 22 m/s

(b) Standard deviation of the normalized velocity in x-direction for HFSB in the XZ-plane at a freestream velocity of 22 m/s

Figure 5.14: Standard deviation of the normalized velocity in x-direction for HFSB in the XY-plane (a) and XZ-plane (b) at a freestream velocity of 22 m/s

5.2.2. Water droplets velocity fields

To see what effect a different freestream velocity has on the behaviour of the water droplets a comparison is made at two velocities. The velocities chosen where 10 and 22 m/s, a comparison of the average flow fields of both cases is shown in figure 5.15. From this comparison it is clear that the coverage of the domain is significantly different between the two cases. While for the 22 m/s case most of the domain is covered, the 10 m/s case barely covers half of the domain. This is caused by the fact that the droplets are not neutrally buoyant due to their high mass compared to air, this means they are pulled to the ground by gravity over time. At lower velocities this means they have dropped more before reaching the model. For this setup this means 10 m/s does not cover the domain around the mirror enough to make a proper analysis. The only conclusion that can be made here is that for further experiments the location of the seeding generator has to be taken into account with the different velocities experiments are done at. For this experiment other locations were not viable, but in other experiments this has to be taken into account when testing at multiple free stream velocities.

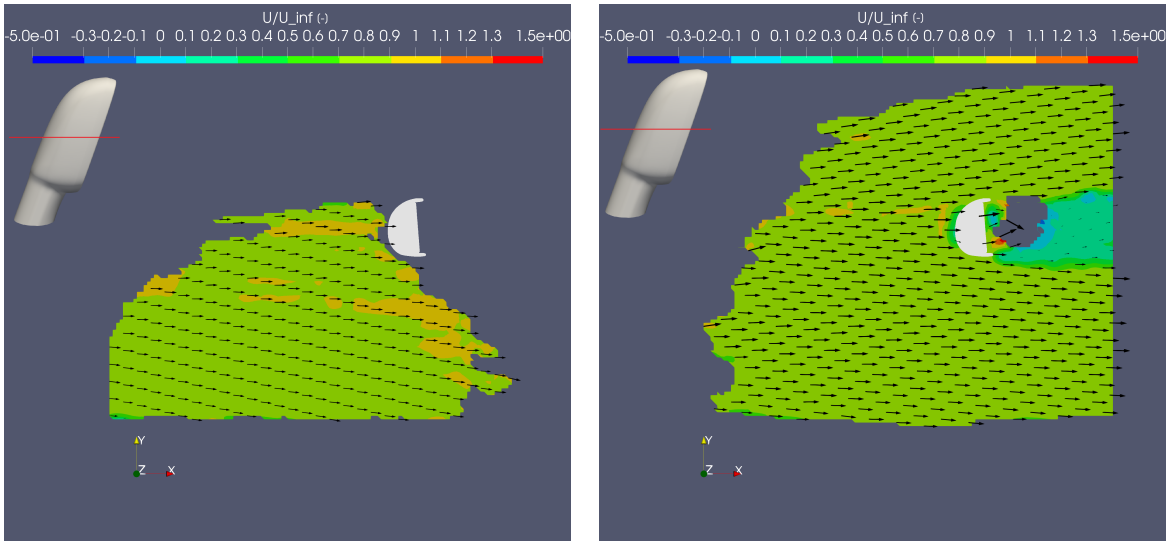

(a) Binning of the Water droplets at a freestream velocity of 10 m/s

(b) Binning of the Water droplets at a freestream velocity of 22 m/s

Figure 5.15: Binning of the Water droplets at a freestream velocity of 10 (a) and 22 (b) m/s

Looking at the concentration of the particles, of which a comparison is shown in figure 5.16, shows a similar picture. The 22 m/s case has a high concentration near the stagnation point, and a larger freestream concentration just below the location of the stagnation point. This already shows that the droplets have fallen a bit. For the 10 m/s case however, the results are significantly worse, a very low concentration of particles is present in front of the mirror, but the further down from the mirror the higher the concentration gets. To see how large the effect is the terminal velocity of the droplets can be calculated by looking at the vertical force balance on a seeding particle, which for simplicity is assumed to be a sphere for these calculations. The three main forces acting on the particle are the gravitational force (equation (5.2)), buoyancy force (equation (5.3)) and drag force (equation (5.4)).

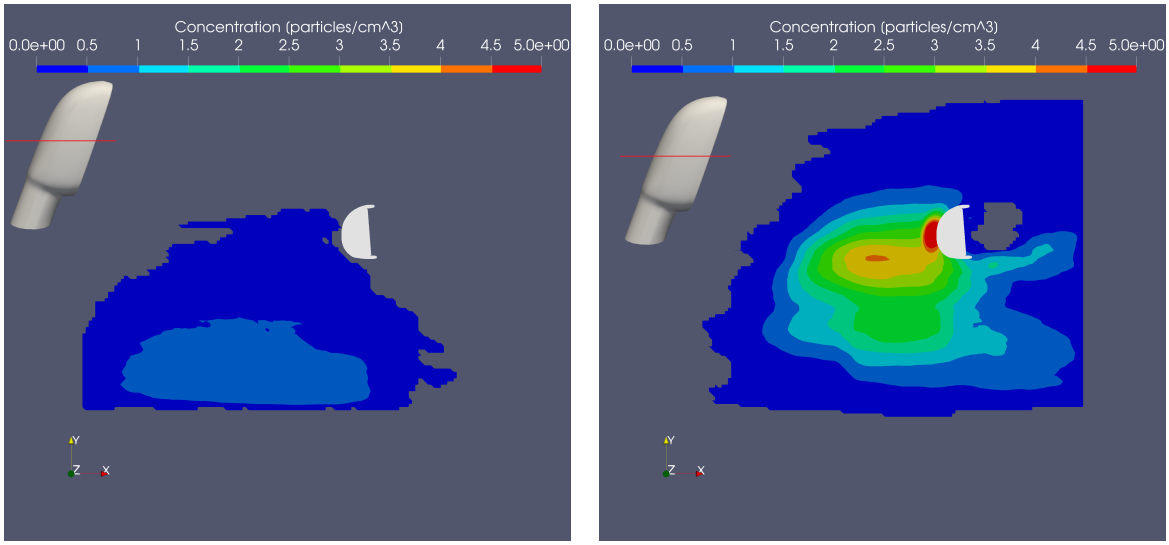

(a) Concentration of the Water droplets at a freestream velocity of 10 m/s

(b) Concentration of the Water droplets at a freestream velocity of 22 m/s

Figure 5.16: Binning of the Water droplets at a freestream velocity of 10 (a) and 22 (b) m/s

$$F_g = \frac{\pi}{6} \cdot d_p^3 \cdot \rho_p \cdot g \tag{5.2}$$

$$F_b = \frac{\pi}{6} \cdot d_p^3 \cdot \rho_f \cdot g \tag{5.3}$$

$$F_d = C_d \cdot \frac{1}{2} \cdot \rho_f \cdot V^2 \cdot A \tag{5.4}$$

where:

- d is the diameter of the spherical particle
- g is the gravitational acceleration
- ρ_p is the density of the particle
- ρ_f is the density of the fluid
- A is the projected area of the spherical particle
- C_d is the drag coefficient of the particle, which for a sphere is equal to 0.47
- V is the velocity of the particle relative to the fluid.

When terminal velocity is reached the gravitational force is balanced out by the buoyancy and drag forces which gives equation (5.5), which can then be rewritten to equation (5.6) using the above definitions. From this equation it is clear that for neutrally buoyant particles ($\rho_p \approx \rho_f$) the terminal velocity approaches zero. Filling in the values of the particle diameter and density for the water droplets ($d = 150\mu m$ and $\rho_p = 997kg/m^3$) gives a terminal velocity of $1.84m/s$. Figure 5.17 shows the vertical velocity of the water droplets in a plane halfway along the mirror. Here it can be seen that the vertical velocity in the freestream below the mirror has a vertical velocity between 0 and -2 m/s (found to average to -0.75 m/s). Assuming this velocity is just reached here means the average velocity in the vertical direction is half of this velocity, being $-0.375m/s$ (assuming linear acceleration). With a distance between nozzle and the mirror of 5 meters this means the droplets will drop by 0.1875 meters at a free stream velocity of $10m/s$ and 0.085 meters as $22m/s$. As a result of the droplets not being in the measurement domain, the 10 m/s experiment's results will not be investigated any further as there is no interesting analysis to be done with this data.

$$F_g = F_b + F_d \tag{5.5}$$

$$V_t = \sqrt{\frac{4g \cdot d}{3C_d} \left(\frac{\rho_p - \rho_f}{\rho_f} \right)} \tag{5.6}$$

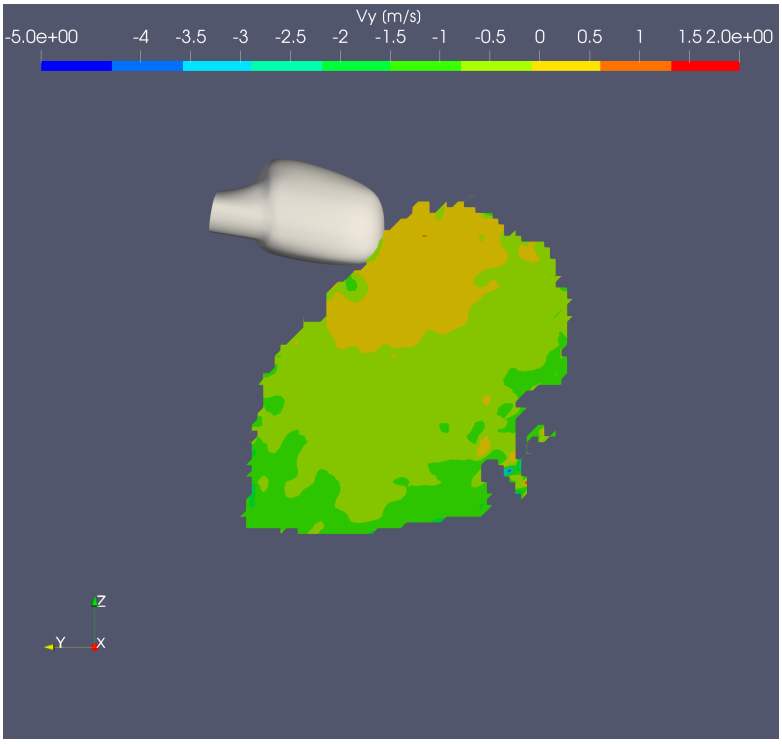

Figure 5.17: Vertical velocity in a plane halfway through the mirror

5.2.3. Comparison of the two models

To see the effect of the different models a comparison is made of the water droplets at a freestream velocity of $22m/s$ as shown in figure 5.18. The first thing that one sees when looking at the comparison is the difference in what parts of the domain are covered by the particles. Most notably also the free stream above the mirror model seems different. To get a better insight in why this is a comparison can be made of the concentrations of both cases, this comparison is shown in figure 5.19. From this it can be seen that while there are droplets above the DrivAer model, it is in a very small concentration, near the limit set for the binning, which was 25. This means it is possible that this was therefore a very small difference that only looks significant due to the processing settings. Another interesting difference is the fact that the concentration of droplets in the freestream seems a lot higher for the DrivAer model, and seems to be more centralized as well. One explanation for this can be the fact that the freestream velocity was a bit slower, when looking back at the binnings of both cases, it can be seen that this is indeed the case, the simple model seems to be in a freestream that is 2-4 m/s slower than the freestream for the DrivAer model, this can then also explain why the concentration above the model drops below the threshold of the processing. Looking specifically at the peak concentration for both cases a significant difference can also be seen. While for the DrivAer model the peak concentration is near the stagnation point of the mirror, the peak for the simple model is below the mirror. One possible explanation for this is the fact that the size of the simple model combined with the flow that is already a bit below center forces the droplets down instead of going to the stagnation point as was the case for the DrivAer model. The last notable difference is the fact that the peak number of particles for the DrivAer model is a lot higher, this is caused by the fact that the droplets tend to impact the model at the stagnation point, where they then tend to break up into smaller particles before sliding along the mirror surface. For the simple model it can be seen that most droplets go under the model instead, therefore they don't impact the model.

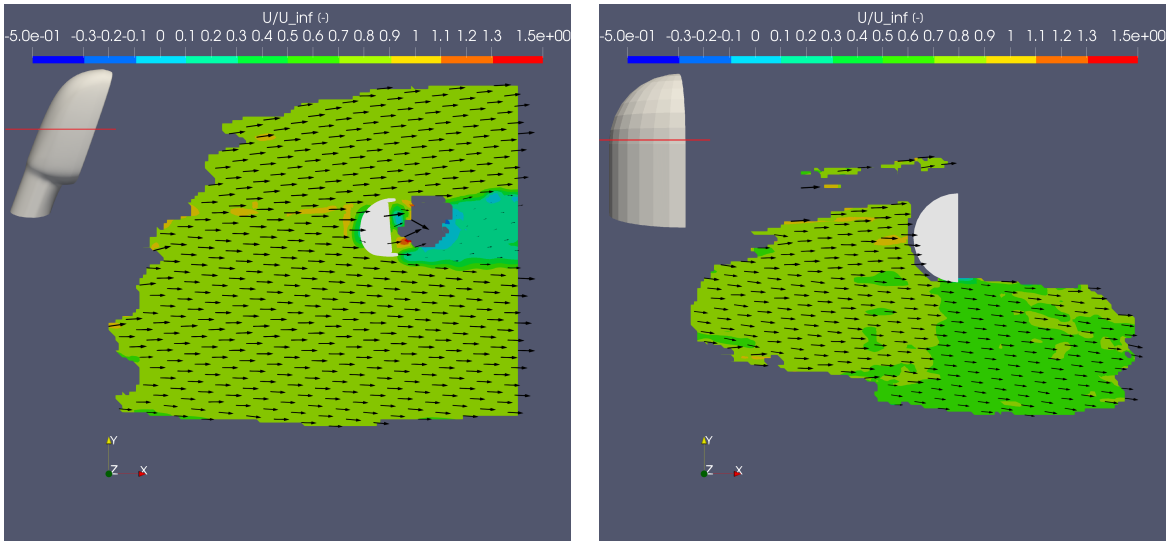

(a) Binning of the water droplets with the DrivAer model at a freestream velocity of $22m/s$.

(b) Binning of the water droplets with the simple model at a freestream velocity of $22m/s$.

Figure 5.18: Comparison of binnings obtained with the DrivAer (a) and simple model (b) at a freestream velocity of $22m/s$

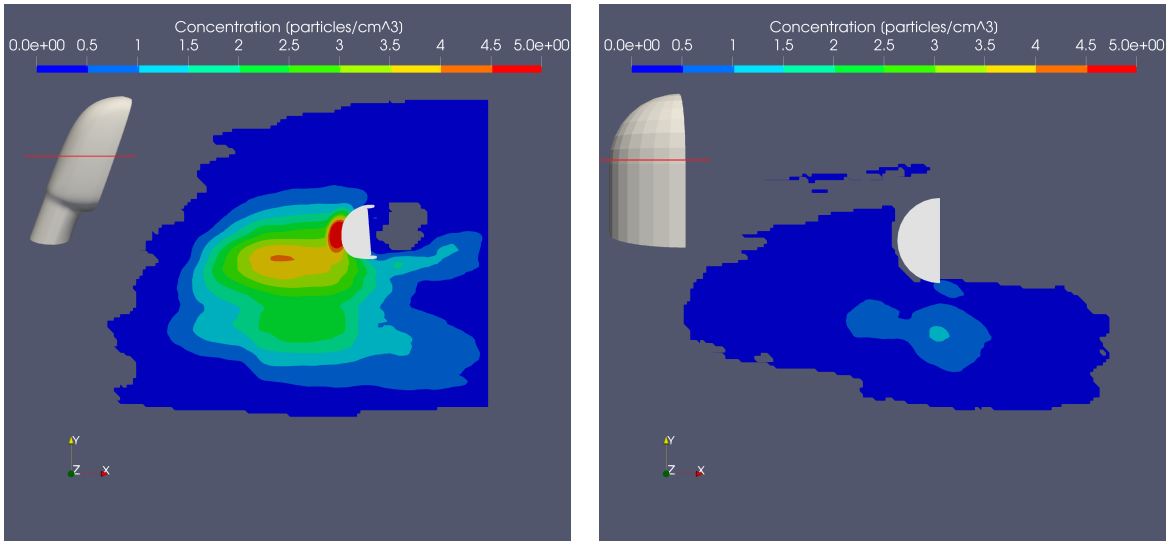

(a) Concentration of the water droplets with the DrivAer model at a freestream velocity of $22m/s$.

(b) Concentration of the water droplets with the simple model at a freestream velocity of $22m/s$.

Figure 5.19: Comparison of concentrations obtained with the DrivAer (a) and simple model (b) at a freestream velocity of $22m/s$

5.2.4. Comparison with HFSB

To give an impression of the amount of particles present in the flow for both the HFSB and water droplets the STB results are shown in figure 5.20. The big takeaway here is that the HFSB has a lot more particles due to the fact it uses the full rake instead of the one nozzle in use for the water droplets.

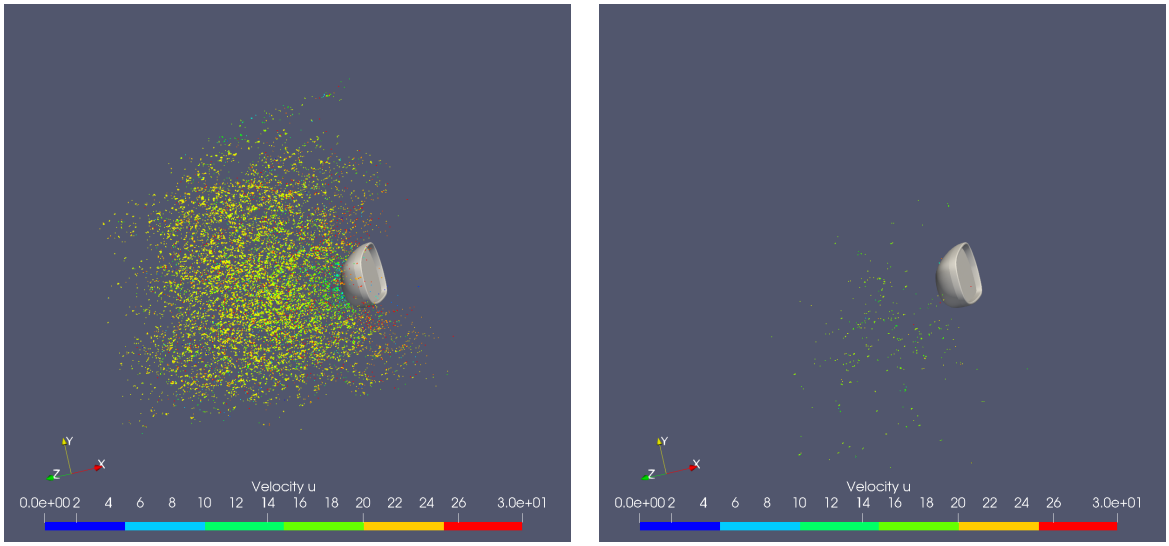

(a) Shake-the-Box HFSB

(b) Shake-the-Box Water droplets

Figure 5.20: Comparison of the STB results obtained with HFSB (a) and water droplets (b)

A comparison can be made for the flow field of the HFSB and water droplets, the binning of the STB results of both tests are shown in figure 5.21a and figure 5.21b. These tests were done at a freestream velocity of $22m/s$, and with the DrivAer side mirror model, and a slice showing the binning was taken at $66mm$ from the plate. To clean up the data, areas with low particle density (1000 per bin for HFSB, 25 per bin for water) were removed; this works fine for the HFSB as with the seeding rake tens of thousands of particles are present. For the water droplets this was not as successful as the seeding concentration is naturally a lot lower at a couple of hundreds of particles per image, so removing these areas quickly led to most of the actual data being removed too. In the end it was chosen to remove enough to reduce most of the noise near the edges of the domain, doing more would reduce the areas which seem to have good data as well. This did cause an area behind the mirror to be removed as well, but that means this area was highly unreliable anyways. This also means that as a result some outliers near the edges and behind the side mirror are still present. As HFSB are proven to track the flow well, the binning of the HFSB can be assumed to be a good representation of the average flowfield present. The flowfield shows a clear deceleration zone when approaching the stagnation point in front of the side mirror, and two acceleration zones near the top and bottom of the side mirror. Comparing this with the results obtained with the water droplets shows that the droplets are moving a bit slower, the HFSB were at a velocity of $22m/s$. The water droplets however are moving at around $18m/s$, most likely due to their large time response. A clear deceleration area can also not be seen, there is a very small area just in front of the mirror which is at a lower velocity, this is however more likely caused by the droplets impacting the model, rather then them actually decelerating in that small area. Similarly no clear acceleration area on top and bottom of the mirror are present. The low velocity area of the water droplets behind the mirror is wider than that of the HFSB, this is due to the ballistic trajectory the droplets tend to take, which causes the droplets to keep a relatively straight path and not follow the flow as it reattaches. This ballistic nature can also be seen by looking at the flow vectors, for HFSB they show the flow around the mirror, whereas for the water droplets they are straight at all points. As droplets impacting the model tend to coalesce on the surface before being released near the top and bottom tips the droplets released there tend to be of larger size as well, which means these droplets are even less affected by the flow. As these large droplets are the main contributors to the flow in the region downstream of the mirror this explains why the low velocity area downstream of the mirror seems to keep a constant width, contrary to the flow.

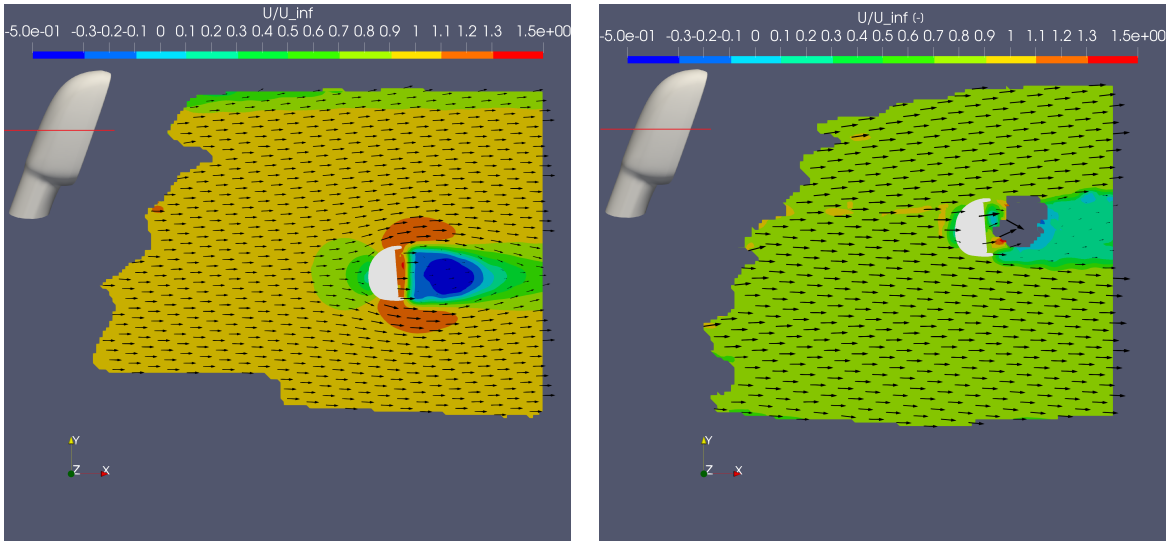

(a) Binning HFSB **(b)** Binning Water droplets

Figure 5.21: Comparison of binnings obtained with the HFSB (a) and Water droplets (b) at z=66 mm

Looking further at the concentrations of both particle types as shown in figure 5.22 significant differences can be seen. First of all the HFSB seems to be more evenly distributed, not only in front of the mirror but also downstream of the mirror. The bottom half of the HFSB shows a higher concentration of bubbles compared to the top half, this is most likely due to an uneven spread produced by the seeding rake, most likely due to nozzles not working properly as sometimes some nozzles clog up for a couple of seconds. The HFSB show a larger concentration nearing the stagnation point. The reason for this is the fact that these concentrations are calculated with the binning data, which means that as a particle slow down it can be present in the same bin area over multiple frames. This means that it is essentially counted multiple times when averaging the data, thereby giving larger concentration values. There seems to also be a very high concentration near the bottom of the mirror, similar behaviour can be seen near the top of the mirror, although less significantly due to the lower overall concentration in that area.

Looking at the standard deviation of the velocity in x-direction for the water droplets as shown in figure 5.23, it can be seen that especially the area behind the mirror is showing a big area with higher standard deviation values. As this is near an area where barely any particles are present, this is most likely caused by low amounts of data, which cause the high fluctuations. One other notable difference when compared with the standard deviations of the HFSB (as shown in figure 5.14) is the fact that the areas emanating from the tips extend a lot more. At a first glance one might assume this means the vortex shedding does affect the droplets, and they just take longer to re-adjust to the freestream. While this certainly can be part of the cause of this, the fact that the droplets are not likely to adept to the vortices shed in the first places makes this unlikely. One has to take into account that there are a lot of droplets impacting the model, these coalesce on the surface, and are released into the freestream in these areas. The size of these droplets is of course not consistent, and therefore their velocities in these areas are also not consistent, explaining the large areas of higher standard deviation here.

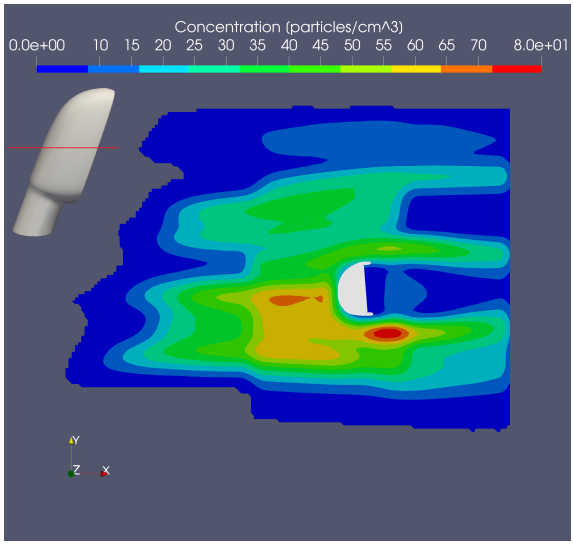

(a) Concentration of the HFSB with the DrivAer model.

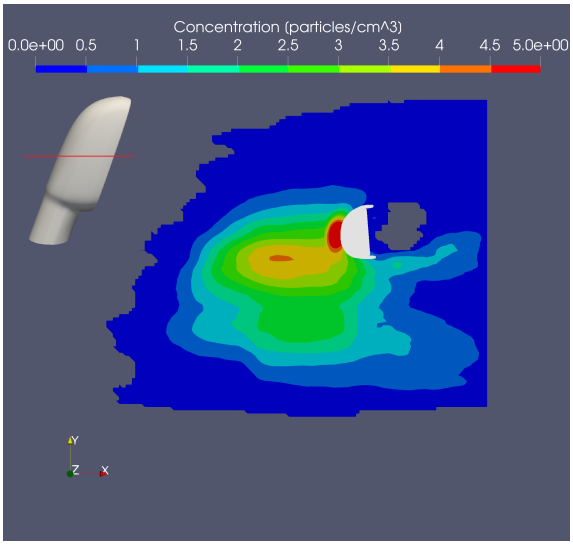

(b) Concentration of the water droplets with the DrivAer model.

Figure 5.22: Comparison of concentrations obtained with the HFSB (a) and Water droplets (b)

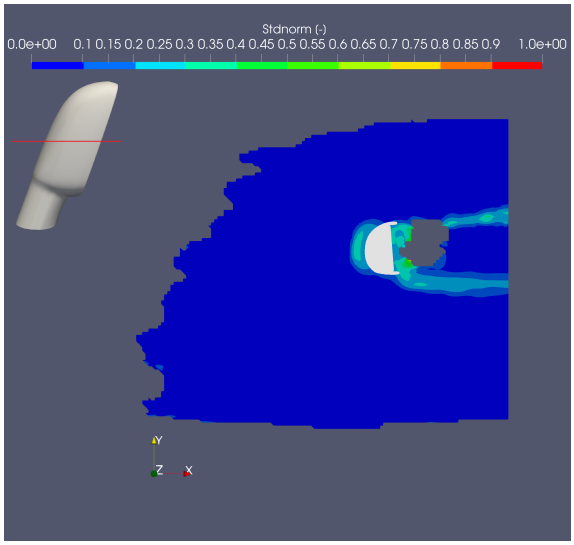

(a) Standard deviation of the velocity in x-direction for Water droplets in the XY-plane

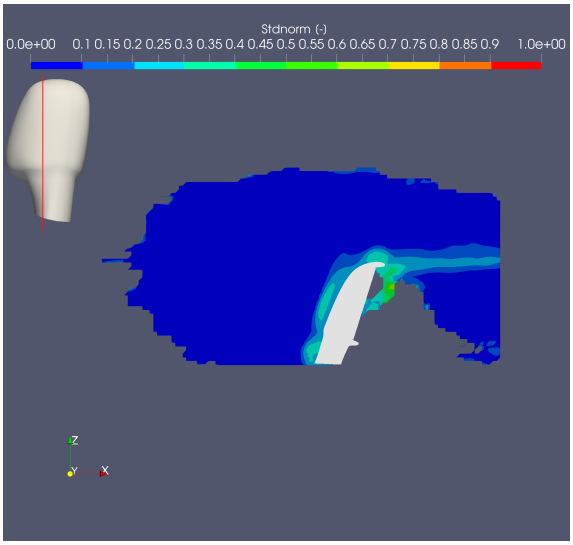

(b) Standard deviation of the velocity in x-direction for Water droplets in the XZ-plane

Figure 5.23: Standard deviation of the velocity in x-direction for Water droplets in the XY-plane (a) and XZ-plane (b)

To show the difference between HFSB and Water droplets in front of the mirror, and in the wake a comparison can be made of the velocity u with respect to y-location. The comparisons for the line in front of the mirror and in the wake are shown in figure 5.24b and figure 5.25 respectively. The planes at which these are done are shown in figure 5.24a, the plane in front (station 1) is 5 mm in front of the mirror, the two behind (station 2 and 3) are at 100 and 170 mm behind the front of the mirror. First of all the difference in freestream velocity of the HFSB and Water droplets is clear from both comparisons, as the HFSB achieve $22m/s$ in the freestream, whereas the Water droplets only achieve $18m/s$. Both the upstream and downstream comparisons at station 2 show that the HFSB are changing their velocity a lot more, indicating that the water droplets, as expected, don't follow the flow properly. It can however be seen that they are affected by the flow in general, the main differences being the severity, as well as the lack of smoothness. The upstream comparison shows the difference in smoothness best, as the

HFSB starts lowering velocity at $y = 100$, whereas the water droplets only start at $y = 50$, giving them a sharper profile compared to the smoother curve of the HFSB. The downstream comparison at station 2 shows the difference in magnitude of the velocity change between HFSB and the Water droplets well. Where the HFSB go from the freestream velocity of $22m/s$ to a velocity of $-10m/s$ in the center of the wake. The water droplets however go from their freestream velocity of $18m/s$ to roughly $2m/s$, which is about half the velocity change the HFSB had in the same area. Comparing the two downstream plots shows that for station 3 further downstream the water droplets actually have a lower velocity compared to the HFSB, it also has this lower velocity over a larger area, this indicates that the 'effective wake' for the water droplets is a lot larger, as they don't adapt to the flow properly, which is to be expected as shown earlier in figure 5.21b.

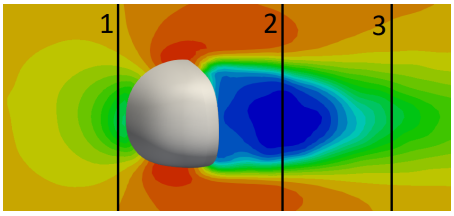

(a) Location of the 3 lines the velocity is plotted along.

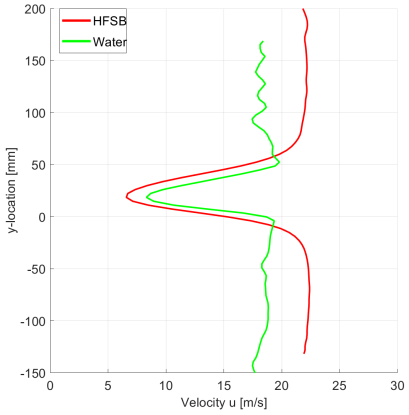

(b) Comparison of the velocity u plotted against the y-location in front of the mirror at station 1

Figure 5.24: Comparison of the velocity u plotted against the y-location at stations 2 and 3

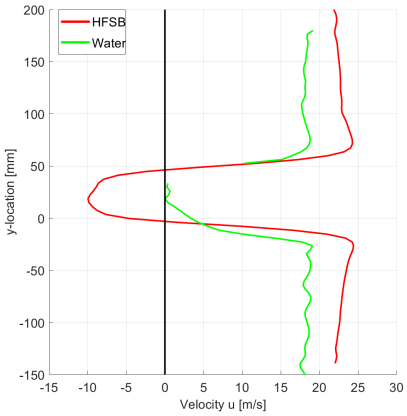

(a) Comparison of the velocity u plotted against the y-location in the wake of the mirror at station 2

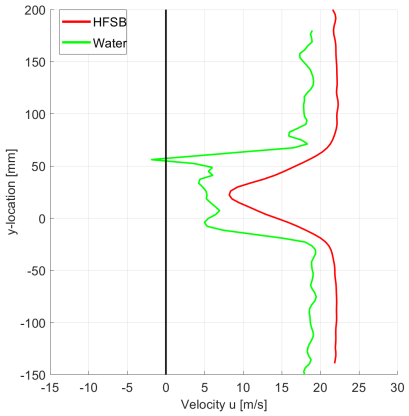

(b) Comparison of the velocity u plotted against the y-location in the wake of the mirror at station 3

Figure 5.25: Comparison of the velocity u plotted against the y-location at stations 2 and 3

From the binning data streamlines can be generated, the comparison of the streamlines are shown in figure 5.26. From this comparison it is again clear that the HFSB flow nicely around the side mirror, whereas the water droplets go straight until they are very close to the side mirror. One thing to note is that the water droplet streamlines are going through the side mirror model, which is most clear in figure 5.26a, this is due to the fact that as previously mentioned, there is unreliable data right behind the mirror that is caused by low seeding density which could not be removed. As a result the streamlines

are generated while trying to fit it to this data as well. This means the streamlines in this area especially need to be taken as irrelevant to the comparison.

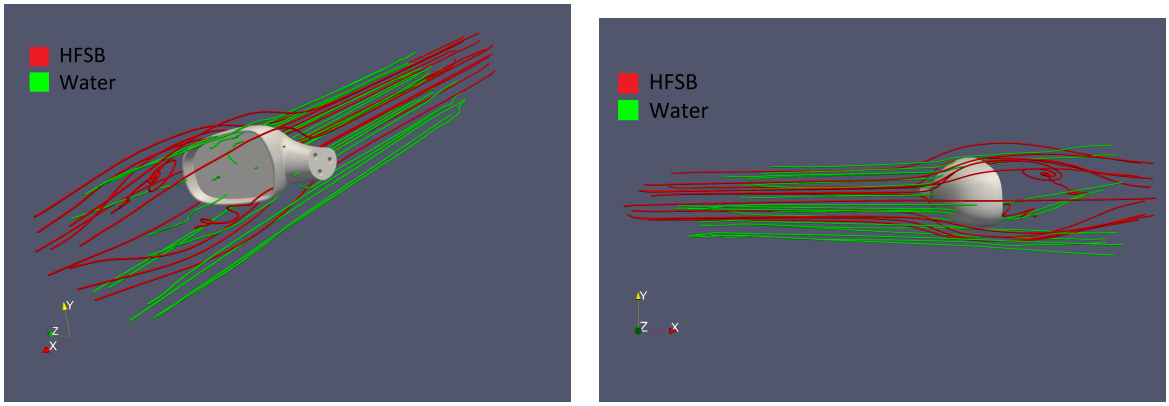

(a) Streamlines 3D

(b) Streamlines Side view

Figure 5.26: Comparison of the streamlines obtained with HFSB and water droplets in a 3D (a) and side view (b)

A good way to see the difference in behaviour of the particles is to compare the velocity and acceleration along a streamline. For both the HFSB and the water droplets one streamline was selected, due to their inherently different behaviour finding an exact same streamline is of course not possible. It was therefore chosen to find streamlines that are in the same point for both particles, the point chosen to be at $x = 0, y = 25, z = 75$. The selected streamlines are shown in figure 5.27, the point where both streamlines cross in front of the mirror is the fixed location that was chosen. The velocity along both streamlines is given in figure 5.28a, the acceleration is given in figure 5.28b the part of the streamlines that are at the location of the mirror and behind are discarded, as indicated by the grey area, because this part is nonphysical (no flow is going through the mirror). The comparison of the velocities shows once more the fact that the water droplets move at a slightly lower velocity compared to the HFSB. The difference in deceleration when approaching the stagnation point is also clear, the HFSB show a very gradual deceleration from x= -50 mm to x= 50 mm, whereas the water droplets don't slow down until they reach the mirror itself. The acceleration graph shows a similar behaviour of both particles, one noteworthy observation is the fact that the water droplets' acceleration seems to fluctuate a lot more than that of the HFSB, near the mirror this is as expected due to them impacting the model. In the freestream however the reason for this is not easily explained, although it could be caused by random fluctuations due to varying droplet sizes here.

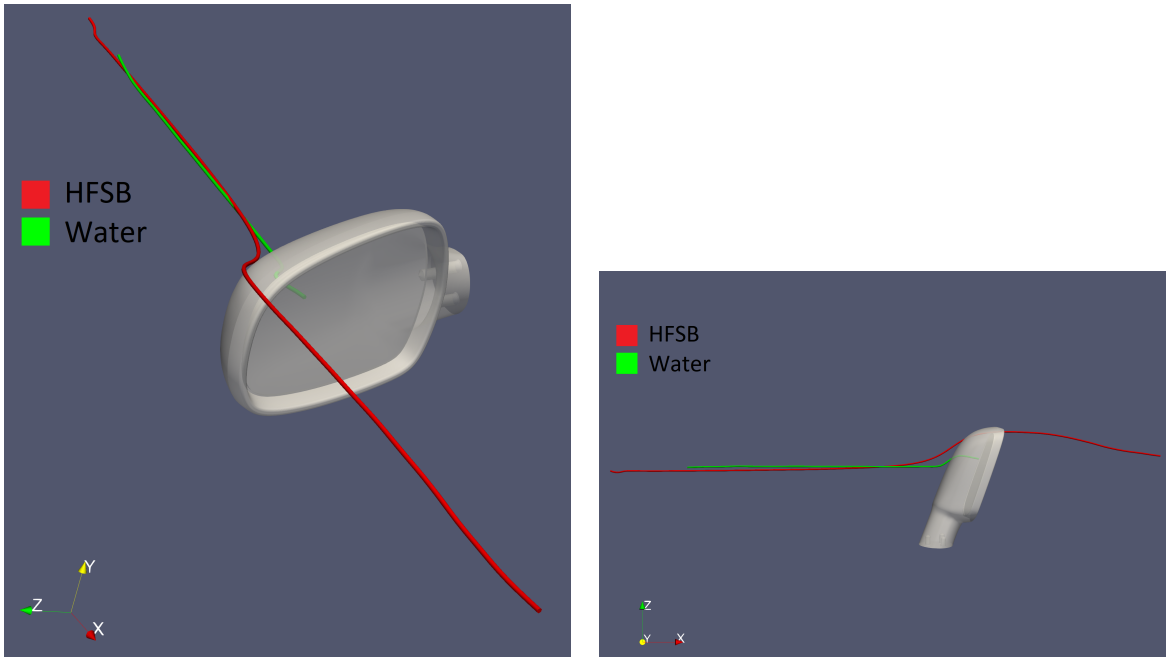

(a) Selected Streamlines 3D

(b) Selected Streamlines Top view

Figure 5.27: Comparison of the streamlines selected for HFSB and water droplets in a 3D (a) and top view (b)

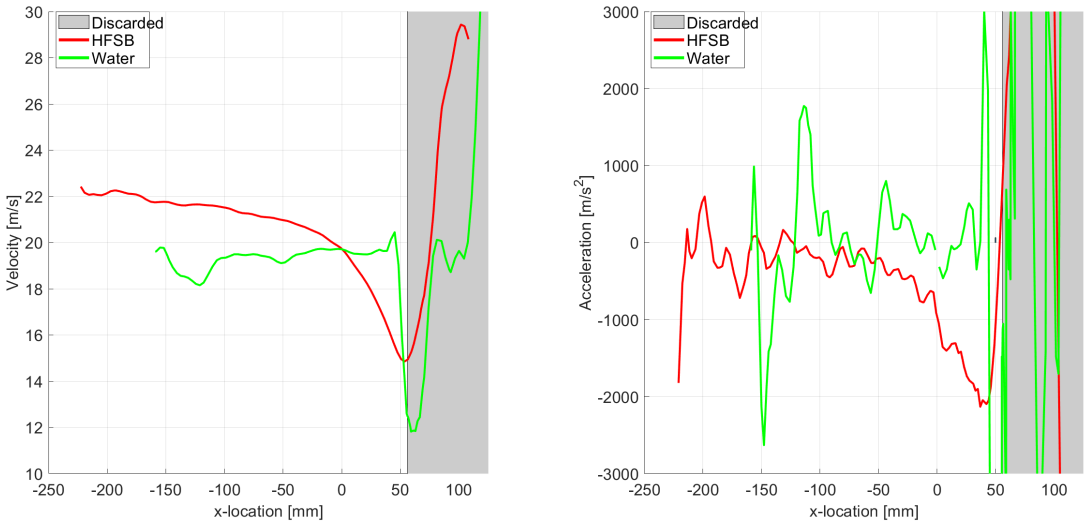

(a) Velocity along the streamline for the HFSB

(b) Acceleration along the streamline for the water droplets

Figure 5.28: Comparison of the velocity (a) and acceleration (b) along the selected streamlines for HFSB and Water droplets

6

Conclusion

The goal of this thesis was to investigate whether water droplets could be used in Particle Image Velocimetry (PIV) experiments with the aim of tracking them for surface contamination research. If possible this would enable new ways of researching surface contamination, which will help ensure safe operation of car sensors used as Advanced Driver Assistance Systems (ADAS).

To investigate the aforementioned goal two experiments have been performed, first a spray characterization experiment was performed to see how well, if at all, the droplets are imaged by the cameras. The second experiment added a car side mirror model to the flow to investigate how the droplets behave in a more realistic scenario. The first experiment showed that the water droplets are able to be detected by the cameras used and are able to be tracked by cross-correlation. The most important caveat observed was the fact that the Arithmic mean Diameter of the water droplets was significantly higher than the nozzle was rated at. This is most likely due to the smaller particles having their glarepoints overlapping, therefore not being recognized as a particle in the diameter calculation script. This meant the script had a bias towards larger particles and therefore could explain this difference. This can be solved by using a more sophisticated diameter calculation script or by setting the experimental parameters such that the smallest particles do not overlap. This last solution is however a bit more complex then it seems, as the absolute size of the water droplets in this experiment was less consistent than that of for example AFSB: $\pm 75mm$ for the water droplets vs $\pm 30mm$ for AFSB. Helium filled soap bubbles (HFSB) are an often used tracer particle in large scale PIV experiments, for this experiment the bubbles were for simplicity filled with air instead, this gave the same imaging properties and only affects their density and thus ability to follow the flow accurately, which was of no concern for this experiment.

The second Experiment introduced a car side mirror model to the flow, during this experiment a comparison was made with HFSB, this can then be used to see how the water droplets behave compared to the flow, which is observed via the HFSB. There have been multiple observations made during this experiment. First of all the water droplets operate at a lower velocity in the free stream compared to the air itself, in this case the windtunnel was operating at $22m/s$, the water droplets however had a velocity of $18m/s$ in the freestream. This means that if one would want to investigate the behaviour of water droplets on a car going at $22m/s$ in a windtunnel the windtunnel needs to operate at a higher velocity. Exactly what velocity the windtunnel needs to be operating at would have to be determined before doing the actual measurements by performing a test run as the exact conditions of the experiment and droplet generating device(s) can have a big impact on this. For an actual running car on a test track this would of course not be an issue, as the car is the one moving at the actual velocity the testing needs to be done. Another observation made was that due to the density of the water droplets being much higher than that of the surrounding air, the droplets have a certain amount of inherent downward velocity, the terminal velocity of the droplets was determined to be $-1.8m/s$, this caused some issues for the experiments at lower freestream velocities. The experiments done at a freestream velocity of $10m/s$ had the droplets fall below the measuring domain, however due to the way the experiment was set up, there was no possibility to alter the location of the spray nozzle, and therefore the

measurements at a freestream velocity of $10m/s$ were of no use. This means that care has to be taken, especially at lower freestream velocities, as to where the water droplets are introduced with respect to the measurement domain to ensure they are present in the measurement domain. The actual tracking of the water droplets showed great promise, not only were the droplets able to be tracked, there were also no detections in the areas where no droplets were expected to be, being directly behind the mirror. Their behaviour in regions of high acceleration/deceleration (nearing the stagnation point of the mirror, and in the wake of the mirror) was also compliant with expectations. The water droplets are slow to adapt to the changes in velocity of the freestream, causing them to not decelerate near the stagnation of the mirror, until they inevitably hit the mirror housing. And in the wake they are slow to adapt to the point where they don't achieve the negative velocities the air does, this also meant they get back to freestream velocity slower than the air does, which in this case was far outside the measurement domain.

From the two experiments it can be seen that the tracking of water droplets with the STB algorithm for the purpose of surface contamination research shows great promise. There needs to be special care taken, especially for windtunnel experiments, to ensure the water droplets are in the right operating conditions and in the right measurement domain, as they don't follow the airflow properly.

To reference back to the research (sub)questions:

- **How effective are water droplets as a seeding particle for surface contamination PIV experiments in combination with the Shake-the-Box algorithm?** The water droplets are shown to be able to work well with the STB algorithm, and therefore show great promise for their use in surface contamination research.

The sub-questions to guide the research to answering the main question are:

- **How well are the cameras able to image the droplets?** There are no large issues with imaging of the water droplets, on caveat here is the fact that these are clean water droplets, droplets with for example dirt in them can alter their reflective properties and potentially cause them to not be imaged at all.
- **How well does the Shake-the-Box algorithm track the droplets over time?** The STB algorithm has shown no issue with tracking the particles over time, all the behavioural properties expected to be shown by the particles were shown in the results obtained by the STB algorithm.
- **How are the trajectories of the water droplets affected by the presence of a model in the flow, such as a side mirror?** The introduction of the side mirror model showed that the droplets trajectory is fairly ballistic as was expected. The droplets impact the model, and are then flowing along the housing before being released at the downstream ends of the mirror into the wake. This leaves a big area directly behind the mirror where no water droplets are present, as was expected.

6.1. Recommendations

Many suggestions for future work can be done based on this thesis, eventually they all boil down to two kinds.

- **Increase of number of nozzles:** The research done in this thesis consisted of using one nozzle in a windtunnel setup, by increasing the size of the experiment further data can be obtained regarding the behaviour of water droplets. Potential ways to scale the experiment up are for example increasing the number of nozzles used. This means that the number of particles per pixel (ppp) is increased, it is shown that for HFSB way higher ppp values are working without issue. For water droplets this can however work a bit differently as due to their ballistic nature and large spread in diameter they can impact each other causing them to break up into smaller droplets, and affecting the ability of the cameras to image them due to reduced amount of light reflected. The other potentially negative effect is the fact that the larger water droplets can be very strong in reflectiveness, thereby obscuring the surrounding droplets. This is not an issue if these particles are rare, but by increasing the amount of nozzles this can potentially also increase the amount of these particles present.

- **Increase of scale:** Another recommendation is increasing the experiment scale, for example by doing a test with a Ring of Fire (RoF) setup, where two cars are following each other through the ring of fire, and then track the droplets sprayed by the first car onto the following car and see how well the water droplets are able to be tracked. This will show how well the particles work in a scenario that would be similar to their intended use case.
- **Different tracer particles:** The research done in this thesis used clear water droplets, in a real life scenario there can be contaminants in the water droplets. These can vary from dirt and cleaning agents to oil and sooth. Depending on how much of these contaminants are present in the droplets the reflectiveness, and therefore there use as tracer particles, can be severely altered. Some experiments can therefore be done with various contaminants, and contamination levels to see how well they are imaged and tracked.

References

[1] M Ashton, P Baas, and Land Transport Safety Authority. *Spray and wind Buffeting from Heavy Vehicles: A literature review*. The Authority, 1998.

[2] M Bannister. *Drag and dirt deposition mechanisms of external rear view mirrors and techniques used for optimisation*. Tech. rep. SAE Technical Paper, 2000.

[3] T Bender, P Hoff, and R Kleemann. *The New BMW Climatic Testing Complex-The Energy and Environment Test Centre*. Tech. rep. SAE Technical Paper, 2011.

[4] S Best, J Komar, and G Elfstrom. "The UOIT Automotive Centre of Excellence-Climatic Test Facility". In: *SAE International Journal of Passenger Cars-Mechanical Systems* 6.2013-01-0597 (2013), pp. 78–87.

[5] A Borg and R Vevang. "On the prediction of exterior contamination with numerical simulations (simple Lagrangian particle tracking methods with and without wall film model)". In: *6th MIRA international conference on vehicle aerodynamics*. 2006, pp. 380–388.

[6] JP Bouchet, P Delpech, and P Palier. "Wind tunnel simulation of road vehicle in driving rain of variable intensity". In: *5th MIRA international conference on vehicle aerodynamics*. 2004.

[7] M. Bühler. "Possibilities for wet road detection for warning against dangerous driving situations". Bachelor thesis. Esslingen, Germany: Hochschule Esslingen, Fakulta¨ t Fahrzeugtechnik, 2012.

[8] C F v Carmer et al. "Identification of vortex pairs in aircraft wakes from sectional velocity data". In: *Experiments in Fluids* 44 (2008), pp. 367–380.

[9] X Chen and W Wang. "The applications of particle image velocimetry (PIV) to experimentally observe the flow behaviors inside the Selective Laser Melting (SLM) working chamber". In: *Flow Measurement and Instrumentation* 73 (2020), p. 101738.

[10] AF Costelli. *Aerodynamic characteristics of the fiat UNO car*. Tech. rep. SAE Technical Paper, 1984.

[11] M S Darms et al. "Obstacle detection and tracking for the urban challenge". In: *IEEE Transactions on intelligent transportation systems* 10.3 (2009), pp. 475–485.

[12] M W Dawley. *Aerodynamic effects on automotive components*. Tech. rep. SAE Technical Paper, 1965.

[13] G E Elsinga et al. "Tomographic particle image velocimetry". In: *Experiments in fluids* 41.6 (2006), pp. 933–947.

[14] GE Elsinga et al. "On the velocity of ghost particles and the bias errors in Tomographic-PIV". In: *Experiments in fluids* 50 (2011), pp. 825–838.

[15] D E Faleiros et al. "Generation and control of helium-filled soap bubbles for PIV". In: *Experiments in Fluids* 60 (2019), pp. 1–17.

[16] T Fersch et al. "The influence of rain on small aperture LiDAR sensors". In: *2016 German Microwave Conference (GeMiC)*. IEEE. 2016, pp. 84–87.

[17] A Filgueira et al. "Quantifying the influence of rain in LiDAR performance". In: *Measurement* 95 (2017), pp. 143–148.

[18] J Fischer et al. "Joint acoustic and wall-pressure measurements on a model A-pillar vortex". In: *Experiments in Fluids* 61 (2020), pp. 1–15.

[19] D M Frey. "WSE-Sensor zur Erkennung feuchter, nasser, schnee-und eisbedeckter Fahrbahnoberflächen". In: ().

[20] Y Fukuchi. "Influence of number of cameras and preprocessing for thick volume tomographic PIV". In: *Proc. 16th Int. Symp. on Applications of Laser Techniques to Fluid Mechanics, Lisbon, Portugal, 9–12 July 2012*. 2012.

[21] A P Gaylard and B Duncan. “Simulation of rear glass and body side vehicle soiling by road sprays”. In: *SAE International Journal of Passenger Cars-Mechanical Systems* 4.2011-01-0173 (2011), pp. 184–196.

[22] A P Gaylard, K Kirwan, and D A Lockerby. “Surface contamination of cars: A review”. In: *Proceedings of the Institution of Mechanical Engineers, Part D: Journal of Automobile Engineering* 231.9 (2017), pp. 1160–1176.

[23] A P Gaylard et al. “Insights into rear surface contamination using simulation of road spray and aerodynamics”. In: *SAE International Journal of Passenger Cars-Mechanical Systems* 7.2014-01-0610 (2014), pp. 673–681.

[24] A Ghasemi, B Ahmet Tuna, and X Li. “Inverse cascade of the vortical structures near the contact line of evaporating sessile droplets”. In: *Scientific Reports* 9.1 (2019), p. 6784.

[25] H Goetz. “The influence of wind tunnel tests on body design, ventilation, and surface deposits of sedans and sport cars”. In: *SAE Transactions* (1971), pp. 854–872.

[26] H Goetz and R Schoch. “Reducing splash and spray of trucks and passenger cars”. In: *SAE transactions* (1995), pp. 1162–1172.

[27] T Hagemeier. “Experimental and numerical investigation of vehicle soiling processes”. PhD thesis. Universitätsbibliothek, 2012.

[28] T Hagemeier, M Hartmann, and D Thévenin. “Practice of vehicle soiling investigations: A review”. In: *International Journal of Multiphase Flow* 37.8 (2011), pp. 860–875.

[29] I Hasirlioglu Sand Doric, C Lauerer, and T Brandmeier. “Modeling and simulation of rain for the test of automotive sensor systems”. In: *2016 IEEE Intelligent Vehicles Symposium (IV)*. IEEE. 2016, pp. 286–291.

[30] Sinan Hasirlioglu et al. “Test methodology for rain influence on automotive surround sensors”. In: *2016 IEEE 19th International Conference on Intelligent Transportation Systems (ITSC)*. IEEE. 2016, pp. 2242–2247.

[31] G Hodgson et al. “An objective measure for automotive surface contamination”. In: *SAE International Journal of Passenger Cars-Mechanical Systems* 11.2018-01-0727 (2018), pp. 341–351.

[32] X Hu et al. “A numerical simulation of wheel spray for simplified vehicle model based on discrete phase method”. In: *Advances in Mechanical Engineering* 7.7 (2015), p. 1687814015597190.

[33] LS Iwan et al. *Transonic Flow Visualization with Neutrally Buoyant Bubbles*. 1973.

[34] J Janson et al. “New development and working methods used in the aerodynamic development of the new large estate”. In: *JSAE paper* 20005352 (2000).

[35] J W Jepson. *Wind-shield cleaner U.S. Patent US1183463A*. 1916.

[36] J Jilesena, A Alajbegovic, and B Duncan. “Soiling and rain simulation for ground transportation vehicles”. In: *7th European-Japanese Two-Phase Flow Group Meeting*. 2015, pp. 11–15.

[37] A Kabanovs et al. “A parametric study of automotive rear end geometries on rear soiling”. In: *SAE International Journal of Passenger Cars-Mechanical Systems* 10.2017-01-1511 (2017), pp. 553–562.

[38] M F Kerho and M B Bragg. “Neutrally buoyant bubbles used as flow tracers in air”. In: *Experiments in Fluids* 16.6 (1994), pp. 393–400.

[39] Lukas Kille et al. *Experimental Investigation of Droplet Formation and Droplet Sizes Behind a Side Mirror*. Tech. rep. SAE Technical Paper, 2022.

[40] T Lajos, L Preszler, and L Finta. “A wind tunnel investigation of mud deposits on the body of a bus”. In: *International Journal of Vehicle Design* 5.6 (1984), pp. 693–703.

[41] *Lan O’lakes Wind tunnels: Jets, bullet trains, race cars and...spray dynamics*. `https://www.landolakesinc.com/Blog/July-2019/winfield-united-wind-tunnel-research-laboratory`. Accessed: 2023-09-13.

[42] LEM Lignarolo et al. “Experimental analysis of the wake of a horizontal-axis wind-turbine model”. In: *Renewable Energy* 70 (2014), pp. 31–46.

[43] *Lufft MARWIS*. https://www.lufft.com/products/road-runway-sensors-292/marwis-umb-mobile-advanced-road-weather-information-sensor-2308/. Accessed: 2023/07/21.

[44] M P Manser, R Koppa, and P Mousley. *Evaluation of splash and spray suppression devices on large trucks during wet weather*. Tech. rep. 2003.

[45] G Maycock. “The problem of water thrown up by vehicles on wet roads”. In: (1966).

[46] M Novara et al. “Lagrangian 3D particle tracking in high-speed flows: Shake-The-Box for multi-pulse systems”. In: *Experiments in fluids* 57 (2016), pp. 1–20.

[47] ME Olson and PR Fry. *Highway tractor-trailer splash and spray reduction through aerodynamic design*. Tech. rep. SAE Technical Paper, 1988.

[48] *Oxford instruments Guide to PIV Mode for iStar sCMOS Camera*. `https://andor.oxinst.com/learning/view/article/piv-mode-for-istar-scmos`. Accessed: 2023-09-13.

[49] D A Plocher and F K Browand. “Comparing spray from tires rolling on a wet surface”. In: *Tire Science and Technology* 42.3 (2014), pp. 145–165.

[50] E Pounder. *Parachute inflation process wind-tunnel study*. Wright Air Development Center, Air Research and Development Command, United …, 1956.

[51] Piatek R and Schmitt J. *Function, safety and comfort. In: Hucho W-H Aerodynamics of road vehicles: from fluid mechanics to vehicle engineering 4th edition.* Warrendale, Pennsylvania: SAE International, 1998.

[52] C Radovich and D Plocher. “Experiments on spray from a rolling tire”. In: *The Aerodynamics of Heavy Vehicles II: Trucks, Buses, and Trains* (2009), pp. 403–417.

[53] R H Rasshofer, M Spies, and H Spies. “Influences of weather phenomena on automotive laser radar systems”. In: *Advances in radio science* 9 (2011), pp. 49–60.

[54] *Road Eye*. https://www.opticalsensors.se/roadeye.html. Accessed: 2023/07/21.

[55] A Scarano Fulvioand Ianiro, K Lynch, and G Cardone. “Time-resolved tomographic PIV investigation of multichannel swirling jets”. In: *Proceedings of the 10th Pacific Symposium on Flow Visualization and Image Processing*. 2015, pp. 1–8.

[56] F Scarano. “Tomographic PIV: principles and practice”. In: *Measurement Science and Technology* 24.1 (2012), p. 012001.

[57] F Scarano et al. “On the use of helium-filled soap bubbles for large-scale tomographic PIV in wind tunnel experiments”. In: *Experiments in Fluids* 56 (2015), pp. 1–12.

[58] D Schanz, S Gesemann, and A Schröder. “Shake-The-Box: Lagrangian particle tracking at high particle image densities”. In: *Experiments in fluids* 57 (2016), pp. 1–27.

[59] D Schanz, M Novara, and A Schröder. “Shake-The-Box particle tracking with variable time-steps in flows with high velocity range (VT-STB)”. In: *Proceedings of 14th International Symposium on Particle Image Velocimetry*. Vol. 1. 1. ILLINOIS Tech/Paul V. Galvin Library. 2021, pp. 1–11.

[60] B Schmiedel. “Road wetness and slipperiness detection for warning against dangerous driving situations”. PhD thesis. Master’s Thesis, RWTH Aachen University, Institut für Kraftfahrzeuge. Aachen …, 2014.

[61] B Schmiedel, F Gauterin, and H Unrau. “Road wetness quantification via tyre spray”. In: *Proceedings of the Institution of Mechanical Engineers, Part D: Journal of automobile engineering* 233.1 (2019), pp. 28–37.

[62] EDR Shearman, E G Hoare, and A Hutton. “Trials of automotive radar and lidar performance in road spray”. In: (1998).

[63] *Siemens 6 inspiring applications of CFD software for vehicle water management*. `https://blogs.sw.siemens.com/simcenter/6-inspiring-applications-of-cfd-software-for-vehicle-water-management/`. Accessed: 2023-09-13.

[64] A Spoelstra et al. “On-site cycling drag analysis with the Ring of Fire”. In: *Experiments in Fluids* 60 (2019), pp. 1–16.

[65] I Spruss. *Ein beitrag zur untersuchung der kraftfahrzeugverschmutzung in experiment und simulation*. Springer, 2016.

[66] I Spruss et al. “Aerodynamics as troubleshooting of wet fading”. In: *ATZ worldwide* 112.10 (2010), pp. 22–25.

[67] W Terra, A Sciacchitano, and F Scarano. “Evaluation of aerodynamic drag of a full-scale cyclist model by large-scale tomographic-PIV”. In: *International workshop on non-intrusive optical flow diagnostics, Delft*. 2016, pp. 25–26.

[68] W Terra et al. “Drag resolution of a PIV wake rake for transiting models”. In: *Experiments in Fluids* 59 (2018), pp. 1–6.

[69] K Thung and P Raveendran. “A survey of image quality measures”. In: *2009 international conference for technical postgraduates (TECHPOS)*. IEEE. 2009, pp. 1–4.

[70] *Torque Can dirt actually protect your car’s paintwork?* `https://www.torque.com.sg/advice/can-dirt-protect-paintwork/`. Accessed: 2023-09-13.

[71] M Trierweiler et al. “Influence of sensor blockage on automotive LiDAR systems”. In: *2019 IEEE SENSORS*. IEEE. 2019, pp. 1–4.

[72] T Waki et al. “Flow visualization around door mirror considering the adhesion of raindrops and wind noise”. In: *JSAE Review* 2.18 (1997), p. 187.

[73] L Walchshäusl et al. “Detection of road users in fused sensor data streams for collision mitigation”. In: *Advanced Microsystems for Automotive Applications 2006*. Springer. 2006, pp. 53–65.

[74] S Watkins. “Spray from commercial vehicles: a method of evaluation and results from road tests”. In: *The Aerodynamics of Heavy Vehicles II: Trucks, Buses, and Trains* (2009), pp. 387–402.

[75] D H Weir, J F Strange, R K Heffley, et al. *Reduction of adverse aerodynamic effects of large trucks, Volume I. Technical report*. Tech. rep. United States. Federal Highway Administration, 1978.

[76] B Wieneke. “Iterative reconstruction of volumetric particle distribution”. In: *Measurement Science and Technology* 24.2 (2012), p. 024008.

[77] B Wieneke. “Volume self-calibration for 3D particle image velocimetry”. In: *Experiments in fluids* 45.4 (2008), pp. 549–556.

[78] V Živkov. *Experimentelle und numerische Untersuchungen der aerodynamischen Kraftfahrzeugeigenverschmutzung*. na, 2004.